




Review

MXene-Based Chemo-Sensors and Other Sensing Devices

Ilya Navitski ^{1,2} , Agne Ramanaviciute ², Simonas Ramanavicius ³, Maksym Pogorielov ^{4,5,*} 
and Arunas Ramanavicius ^{2,*} 

¹ Department of Nanotechnology, State Research Institute Center for Physical Sciences and Technology (FTMC), Saulėtekio av. 3, LT-10257 Vilnius, Lithuania; ilya.nov42@gmail.com

² Department of Physical Chemistry, Faculty of Chemistry and Geosciences, Institute of Chemistry, Vilnius University, Naugarduko 24, LT-03225 Vilnius, Lithuania; agne.ramanaviciute@gmail.com

³ Department of Organic Chemistry, State Research Institute Center for Physical Sciences and Technology, Saulėtekio av. 3, LT-10257 Vilnius, Lithuania; simonas.ramanavicius@ftmc.lt

⁴ Biomedical Research Centre, Sumy State University, 2, Kharkivska Str., 40007 Sumy, Ukraine

⁵ Institute of Atomic Physics and Spectroscopy, University of Latvia, 3 Jelgavas St., LV-1004 Riga, Latvia

* Correspondence: maksym.pogorielov@lu.lv (M.P.); arunas.ramanavicius@chf.vu.lt (A.R.)

Abstract: MXenes have received worldwide attention across various scientific and technological fields since the first report of the synthesis of Ti_3C_2 nanostructures in 2011. The unique characteristics of MXenes, such as superior mechanical strength and flexibility, liquid-phase processability, tunable surface functionality, high electrical conductivity, and the ability to customize their properties, have led to the widespread development and exploration of their applications in energy storage, electronics, biomedicine, catalysis, and environmental technologies. The significant growth in publications related to MXenes over the past decade highlights the extensive research interest in this material. One area that has a great potential for improvement through the integration of MXenes is sensor design. Strain sensors, temperature sensors, pressure sensors, biosensors (both optical and electrochemical), gas sensors, and environmental pollution sensors targeted at volatile organic compounds (VOCs) could all gain numerous improvements from the inclusion of MXenes. This report delves into the current research landscape, exploring the advancements in MXene-based chemo-sensor technologies and examining potential future applications across diverse sensor types.

Keywords: MXenes; strain sensors; pressure sensors; temperature sensors; humidity sensors; gas sensors; 2D nanomaterials; volatile compounds; MAX phase; energy storage



Citation: Navitski, I.; Ramanaviciute, A.; Ramanavicius, S.; Pogorielov, M.; Ramanavicius, A. MXene-Based Chemo-Sensors and Other Sensing Devices. *Nanomaterials* **2024**, *14*, 447. <https://doi.org/10.3390/nano14050447>

Academic Editors: Antonino Gulino and Dong-Joo Kim

Received: 10 January 2024

Revised: 15 February 2024

Accepted: 24 February 2024

Published: 28 February 2024



Copyright: © 2024 by the authors. Licensee MDPI, Basel, Switzerland. This article is an open access article distributed under the terms and conditions of the Creative Commons Attribution (CC BY) license (<https://creativecommons.org/licenses/by/4.0/>).

1. Introduction

The family of two-dimensional (2D) transition metal carbides, nitrides, and carbonitrides called MXenes has significantly grown since the first report of the synthesis of Ti_3C_2 in 2011 [1]. In recent years, MXenes have greatly impacted many fields, including energy storage [2,3], electronics [4,5], biomedicine, catalysis [6,7], environmental technologies, and many other technological areas. This widespread attention arises from the exceptional set of properties attributed to MXenes, which include superior mechanical strength and flexibility [8], liquid-phase processability [9], tunable surface functionality [10], high electrical conductivity [11], and the ability to customize their properties. This array of highly functional and desirable material qualities inevitably led to the production of thousands of publications during the previous ten years [12]. MXenes are characterized by the general chemical formula $\text{M}_{n+1}\text{X}_n\text{T}_x$, where M is one of the transition metals, n varies from 1 to 4 [13], X indicates C and/or N, and T_x denotes the surface terminations, which include $-\text{F}$, $-\text{O}$, and $-\text{OH}$ as well as other chalcogens ($-\text{S}$, $-\text{Se}$, $-\text{Te}$), halogens ($-\text{Cl}$, $-\text{Br}$, $-\text{I}$), or imido ($=\text{NH}$) groups [14,15]. The suffix “ene” underscores their structural similarity to graphene and to other 2D materials [16]. Figure 1 shows the elements of the known MAX phases and MXenes.

A

$M_{n+1}X_nT_x$

H																			He
Li	Be											B	C	N	O	F			Ne
Na	Mg											Al	Si	P	S	Cl			Ar
K	Ca	Sc	Ti	V	Cr	Mn	Fe	Co	Ni	Cu	Zn	Ga	Ge	As	Se	Br			Kr
Rb	Sr	Y	Zr	Nb	Mo	Tc	Ru	Rh	Pd	Ag	Cd	In	Sn	Sb	Te	I			Xe
Cs	Ba	Lu	Hf	Ta	W	Re	Os	Ir	Pt	Au	Hg	Tl	Pb	Bi	Po	At			Rn
Fr	Ra	Lr	Rf	Db	Sg	Bh	Hs	Mt	Ds	Rg	Cn	Nh	Fl	Mc	Lv	Ts			Og
		La	Ce	Pr	Nd	Pm	Sm	Eu	Gd	Tb	Dy	Ho	Er	Tm	Yb				
		Ac	Th	Pa	U	Np	Pu	Am	Cm	Bk	Cf	Es	Fm	Md	No				

B

$M_{n+1}AX_n$

H																			He
Li	Be												B	C	N	O	F		Ne
Na	Mg												Al	Si	P	S	Cl		Ar
K	Ca	Sc	Ti	V	Cr	Mn	Fe	Co	Ni	Cu	Zn	Ga	Ge	As	Se	Br			Kr
Rb	Sr	Y	Zr	Nb	Mo	Tc	Ru	Rh	Pd	Ag	Cd	In	Sn	Sb	Te	I			Xe
Cs	Ba	Lu	Hf	Ta	W	Re	Os	Ir	Pt	Au	Hg	Tl	Pb	Bi	Po	At			Rn
Fr	Ra	Lr	Rf	Db	Sg	Bh	Hs	Mt	Ds	Rg	Cn	Nh	Fl	Mc	Lv	Ts			Og
		La	Ce	Pr	Nd	Pm	Sm	Eu	Gd	Tb	Dy	Ho	Er	Tm	Yb				
		Ac	Th	Pa	U	Np	Pu	Am	Cm	Bk	Cf	Es	Fm	Md	No				

Figure 1. Elements of the known MXenes (A) and MAX phases (B).

One of the many reasons why MXenes are used in a variety of industries is the diverse chemistry associated with the element “M”. For instance, Vanadium (V)-based MXenes have a low ion diffusion barrier and some characteristics required for energy storage devices [17], Molybdenum (Mo)-based MXenes have great potential for application in the fields of electrocatalysis and thermoelectricity [18], and Niobium (Nb)-based MXenes exhibit magnetic phase change due to their diamagnetic nature [19]. However, $Ti_3C_2T_x$ remains the most studied and commonly used MXene.

Etching the “A” element from the MAX phase, which is represented by the formula $M_{n+1}AX_n$, is a common step in the MXene synthesis process [20,21]. HF etching is the most popular etching technique, which is applied for the preparation of MXenes from a particular MAX phase [22–25]. However, the primary issue with this approach is the corrosive and hazardous nature of HF, which raises concerns about potential harm to the environment and public health. To overcome this issue, scientists have recently developed a number of innovative etching methods. Alkali etching [26,27], molten salt etching [28,29], electrochemical etching [30,31], iodine etching [32] and UV-induced etching [33] are some of the many new approaches for synthesizing MXenes. After the etching, multilayered MXenes are created and can already be utilized in some applications (such as lubrication [34]). However, in many other cases, MXenes must be intercalated and delaminated in order to optimize the chemical characteristics of these materials. DMSO [35], bases such TBAOH [36] and isopropylamine [37], and a variety of cations (Li^+ [13], Na^+ [38], K^+ and others [23]) are used as intercalants during the delamination of MX phase and the formation of 2D MXene sheets. Figure 2 shows a schematic depiction of Nb_2CT_z MXene synthesis, depicting all major steps necessary for MXene formation.

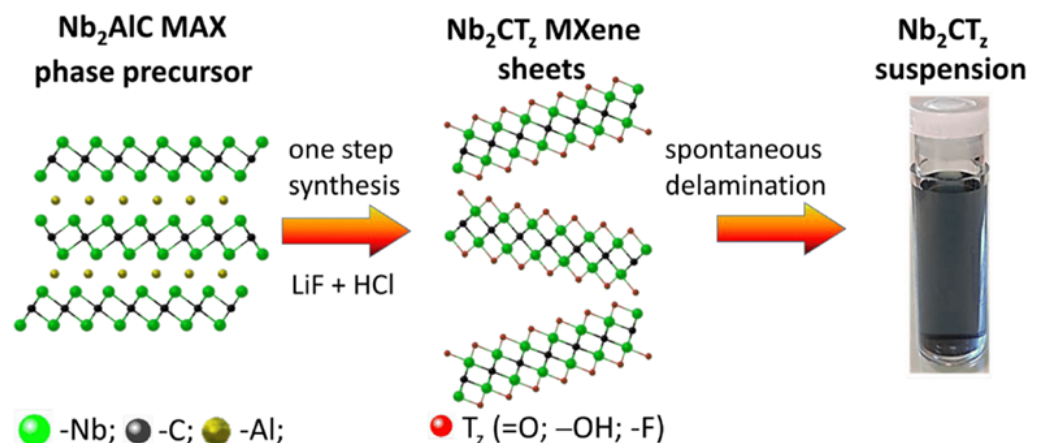


Figure 2. Schematic depiction of Nb₂CT₂ MXene synthesis. Reprinted from [39].

MAX phases are usually produced by combining laboratory-grade elemental powders (Ti, Al, and C powders for Ti₃AlC₂) and heating the mixture in an inert atmosphere to extreme temperatures; as such, this makes the production of the precursor relatively expensive compared to other two-dimensional substances (in comparison to obtaining graphene from graphite). Consequently, MXene production is comparatively expensive [40]. As a result, the developments in some areas may be hindered as it becomes economically unfeasible. Some research groups were able to synthesize MAX phases using inexpensive components (such as TiO₂, Al from scrap metal, and C recovered from tires) and then utilize the obtained product to create MXenes. The comparison of properties between MXenes made from pure MAX phases and the ones from the inexpensive precursors exhibited similarities that are sufficient for certain applications. This shows that much more affordable MXene synthesis can be achieved and successfully applied as well [40,41]. However, for many other fields, especially ones that require highly pure MXenes, further improvements in synthesis are still needed.

MXenes are among the greatest materials that are used for sensing applications due to their various properties and the ability to tune them for users' purposes by changing "M", "T_x" or the number of layers [42]. The addition of MXenes to sensor designs can improve strain sensors, temperature sensors, pressure and gas sensors and chemical sensors. Therefore, the aim of this report is to examine the state of research and potential future applications of some MXene-based sensors. In this paper, we discuss the benefits that MXenes can provide to different types of sensors, examine the mechanisms or reactions behind the sensing, and highlight the most unique and interesting works of the past decade. The main focus will be placed on outlining fairly recent (2022–2023) and, in our opinion, the most exciting advancements in the aforementioned sensor types. Moreover, the review will focus not only on the most popular Ti₃C₂T_x sensors but also on other novel MXene applications. It must be noted that biosensing applications of MXenes will not be discussed due to the enormously wide scope of this particular topic.

2. MXene-Based Strain Sensors

The rapid advancement of flexible electronics-based devices in recent years has led to their widespread adoption across numerous industries. These devices, characterized by their bendable and conformable nature, have unlocked new possibilities and applications in fields such as sports, communications, medicine, and beyond. The versatility of flexible electronic devices has spurred innovation and opened new avenues for interdisciplinary research. As technology continues to advance, it is likely that flexible electronics will play an even more significant role in shaping the future of various industries [43]. For wearable applications like human motion detection, strain sensors need to meet several baseline requirements, including high stretchability, flexibility, sensitivity, and durability. To achieve

this, scientists need to carefully design and coordinate different materials. One method is to insert zero-dimensional nanoparticles, such as metal nanoparticles [44,45], into an elastic substrate to create a conductive network, which can help in achieving high sensitivity. However, steady sensing may be hampered by the instability of the conductive network. On the other hand, one-dimensional nanowires like CNTs [46,47] and AgNWs [48] can be used to create a conductive network inside or on top of the elastic substrate. Because of the relatively stable conductive channels provided by this construction, resistance changes are less likely to occur due to deformation, yet this comes at a cost of decreased sensitivity [49]. Contrary to most other two-dimensional materials, such as graphene, MXenes have a large initial metallic conductivity. Since the crack propagation mechanism (Figure 3) dominates the sensing, MXene-based strain sensors exhibit increased resistance during stretching [50]. A narrow sensing range is the result of MXene sheets' tendency to lose inter-sheet connections during the tensile process [51–53]. Combining conductive materials can enhance the overall conductivity and performance by taking advantage of different qualities of the materials.

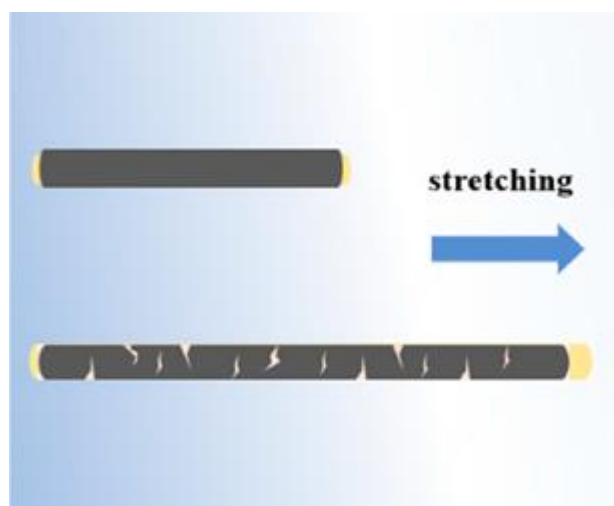


Figure 3. Schematic illustration of the crack propagation mechanism behind MXene-based strain sensors. Reprinted from [54].

One of the profound features of MXenes in strain sensor design is the ability to tune properties, such as the sensitivity and working area. $\text{Ti}_3\text{C}_2\text{T}_x$ An MXene/carbon nanotube (CNT) composite was conceptually designed and included in strain sensors by Yichen Cai et al. CNT crossing and $\text{Ti}_3\text{C}_2\text{T}_x$ nano-stacks were combined in a weaving architecture. The resulting strain sensor had an ultralow detection limit of 0.1% strain, tunable sensitivity (gauge factor up to 772.6), and customizable sensing range, mostly depending on the concentration ratio between CNT and MXene (30% to 130% strain) [52]. Wireless $\text{Ti}_3\text{C}_2\text{T}_x$ MXene strain sensing devices were created by Haitao Yang et al. Within several user-specified high-strain working windows (from 130% to 900%), the wireless MXene sensor system may simultaneously achieve an ultrahigh sensitivity (with gauge factor up to 14,000) and reliable linearity ($R^2 = 0.99$). The authors used a single database channel by the wireless system to track all of the exoskeleton actuations [55].

Due to the hydrophilicity of MXenes, based on surface terminations, they can be implemented in hydrogels. Figure 4 shows a schematic illustration of the mechanism of MXene-based hydrogel strain sensors. Hui Liao et al. immersed MXene nanocomposite hydrogel (MNH) into ethylene glycol to create an anti-freezing, self-healing, and conductive MNOH. According to the authors, MNOH may be incorporated into a wearable strain sensor with a reasonably wide strain range (up to 350% strain) and a high gauge factor of 44.85 under very low temperatures to monitor human biological activity [56].

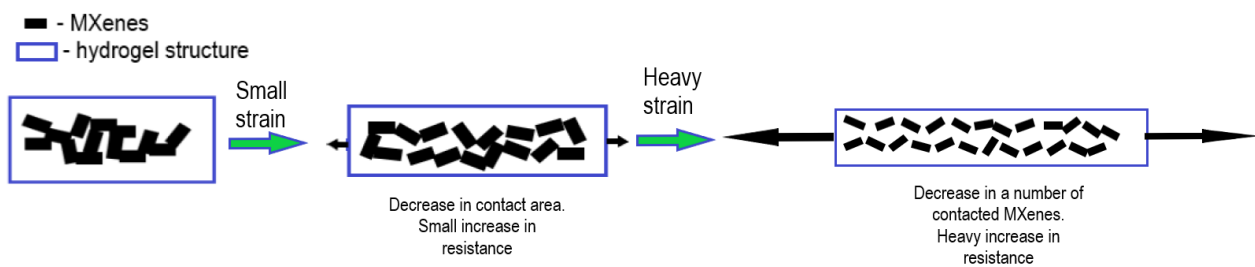


Figure 4. Schematic illustration of the mechanism behind MXene-based hydrogel strain sensors.

In 2023, Chunqing Yang et al. created a sandwich-structured flexible strain sensor using MXene, polypyrrole, hydroxyethyl cellulose (MXene/PPy/HEC), and a flexible substrate made of PDMS. The signals of handwritten Chinese, Arabic, and English words measured by the sensor exhibited distinctive properties. Different handwritten characters were successfully recognized by the authors using machine learning techniques, with a recognition accuracy above 96% [57].

In conclusion, MXenes, especially $Ti_3C_2T_x$, have been successfully applied in strain sensor design due to their superior electrochemical properties, metallic conductivity, and hydrophilicity. They are able to provide high sensitivity to strain sensors at the cost of narrowing the working area. More examples of MXene usage in strain sensors can be found in Table 1.

Table 1. MXene application in strain sensors.

Composition	Sensitivity (GF)	Test Range, Strain %	LOD, Strain %	Ref
$Ti_3C_2T_x$ /MWCNTs/TPU	13–363	0–100	-	[58]
$Ti_3C_2T_x$ MXene/polyurethane	22.9–228	58–150	0.1	[59]
CNT/ $Ti_3C_2T_x$ MXene/PDMS	13.3	0–60.3	-	[53]
MXene/PANIF	97.6–2369.1	0–80	0.1538	[60]
$Ti_3C_2T_x$ MXene/paper	17.4	0–0.6	0.1	[61]
$Ti_3C_2T_x$ MXene/P(VDF-TrFE)	6.35–108.8	45–66	-	[62]
PVA/CMC/TA/MXene hydrogel	2.9	0–700	1	[63]
PVA-CA-MXene hydrogel	2.3	0–200	-	[64]
Polyvinyl alcohol/polyacrylamide/ $CaCl_2$ /MXene	3.0	0–300	-	[65]
Liquid metal/MXene	7.85–15.47	0–400	-	[66]
PAA/PEDOT:PSS/MXene hydrogel	9–20.86	0–1000	-	[67]
MXene/AgNWs/TPU	33.1	0–120	-	[68]

3. MXene-Based Pressure Sensors

Flexible pressure sensors have become integral components in wearable electronic devices, offering a wide range of applications in areas such as health monitoring, human-machine interfaces, and robotics. In the past decade, numerous studies have focused on exploring various mechanisms employed in flexible pressure sensors, including piezoresistive, piezocapacitive, piezoelectric, and triboelectric principles. These mechanisms enable these sensors to detect and respond to pressure changes in different ways. The Piezoresistive mechanism involves changes in the electrical resistance as a response to mechanical deformation. Flexible pressure sensors using piezoresistive materials, such as certain polymers or carbon-based composites, can detect pressure by measuring variations in resistance [69]. The Piezocapacitive mechanism is mostly based on monitoring the capacitance changes, which are generated in response to pressure and are the basis of piezocapacitive sensors. These sensors typically consist of flexible materials with varying capacitance, and the pressure-induced deformations lead to changes in the capacitance that can be measured [70]. The Piezoelectric mechanism is realized in materials with piezoelectric properties to generate an electric charge in response to mechanical stress. Flexible pressure

sensors based on the piezoelectric mechanism use such materials to convert pressure-induced deformations into electrical signals [71]. Triboelectric sensors generate electric charges through the triboelectric effect, which involves the transfer of electrons between materials in contact. Flexible pressure sensors based on triboelectric principles can detect pressure changes through the generation of triboelectric charges [72]. All these mechanisms offer different advantages and are suitable for various applications based on the specific requirements of the wearable device. The choice of the mechanism depends on factors such as the required sensitivity, response time, and the overall design of the sensor. The ongoing research and development in this field aims to improve the performance, sensitivity, and flexibility of these pressure sensors, contributing to the continued evolution of wearable electronic devices and their integration into diverse applications [73–77]. Piezoresistive pressure sensors stand out among the others due to the ease of device assembly and the comparatively low requirements for signal collection and readout [78]. The structure of all types of pressure sensors consists of flexible substrates, active materials, and conductive electrodes despite the fact that different sensing mechanisms are used. High sensitivity, a wide detection range, rapid response time, low detection limit, and good linearity are required for the perfect flexible pressure sensor [79–81]. However, because of the constrained sensing capabilities and intricate manufacturing process, the practical application of pressure sensors is still challenging and expensive. A brand-new frontier in the development of pressure sensors has been opened by the discovery of MXenes and especially $\text{Ti}_3\text{C}_2\text{T}_x$ -based ones. The surface of $\text{Ti}_3\text{C}_2\text{T}_x$, in contrast to other 2D materials like graphene and black phosphorus, has a great number of attached exchangeable functional groups, which gives them exceptional water dispersion and plasticity. They may also be mixed with other materials to create a variety of multifunctional arrangements and micro-structures. $\text{Ti}_3\text{C}_2\text{T}_x$ nanosheets are noteworthy due to their advantageous mechanical properties, high conductivity, and pressure-adjustable layer spacing. These features offer a solid foundation for the design of microstructures, which are required for pressure sensors, tactile sensors, and the formation of force-sensing layers [82]. Figure 5 shows the mechanism behind MXene-based pressure sensors.

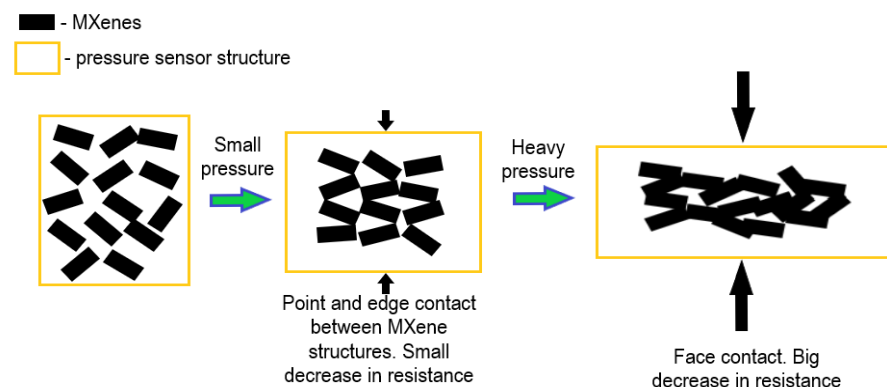


Figure 5. Schematic illustration of the mechanism behind MXene-based pressure sensors.

An MXene/cotton fabric (MCF)-based pressure sensor was developed in 2020 by Yanjun Zheng et al., utilizing the flexibility and three-dimensional porous structure of cotton fabric as well as the unique sandwich construction of the sensor. It displayed advanced stability, long-term durability, high sensitivity (5.30 kPa^{-1} in the pressure range of 0–1.30 kPa), a wide sensing range (0–160 kPa), and a quick response/recovery time (50 ms/20 ms) [83]. A flexible, extremely sensitive, and waterproof sponge pressure sensor was described by Zhenyuan Xu et al. SiO_2 , MXene, and NH_2 -CNTs were put together to create the sensor on a melamine sponge core. Good sensitivity (10.8 kPa^{-1}), a quick response and recovery time (40 ms and 60 ms, respectively), a broad detection range (30 kPa), and a remarkably low detection limit (4.6 Pa) were all features of this waterproof sponge pressure sensor [84]. Lin Wang et al. created an MXene/ANFs composite aerogel

through a controlled vacuum filtering procedure followed by freeze-drying. The aerogel sensor exhibited a broad detection range (2.0–80.0% compression strain), good sensitivity (128 kPa^{-1}), and a low detection limit (100 Pa) [85]. In 2022, Tingting Yin et al. developed MXene/polyaniline (PANI) foam utilizing a steam-induced foaming technique to produce a 3D porous structure. This foam-based sensor demonstrated exceptional wear resistance (10,000 cycles), quick response and recovery times (106/95 ms), and remarkable sensitivity (690.91 kPa^{-1}) [86]. In 2022, using electrospinning technology, Xiyao Fu et al. created a pressure sensor using the MXene/ZIF-67/polyacrylonitrile (PAN) nanofiber film. The film-based device exhibited a broad operating range (0–100 kPa), good sensitivity (62.8 kPa^{-1}), robust mechanical stability (over 10,000 cycles), and a quick response/recovery time (10/8 ms) [81].

Sound, which is essentially a ‘vibration’ of molecules, may travel through a gaseous/liquid/solid medium and can be transmitted as mechanical waves based on the variation of pressure and motion [87]. Exploring communication systems that use other modes of signals instead of sound is important as various human infirmities can restrict or impede the capacity to talk [88]. Compared to layered graphene or other materials, MXene nanoflakes with considerably varied interlayer spacing may produce a higher mechanical response, making them an appropriate mechanical sensing material for developing piezoresistive devices for sound registration [89]. Yangyang Pei et al. used foamed MXenes for their sound sensor. This method enabled this group of scientists to tackle the MXenes’ self-stacking problem, a common limitation that restricts material applications, by reducing the total energy. The $\text{Ti}_3\text{C}_2\text{T}_x$ -based sensor demonstrated exceptional durability over 5000 cycles, a low detection limit of 1 Pa, a quick reaction time of 132 ms, and an impressive sensitivity of 102.89 kPa^{-1} for pressures less than 1 kPa. The sensor demonstrated the ability to perceive air pressure waves as an eardrum, distinguishing between diverse natural sounds and identifying human voices [90]. Guang-Yang Gou and others reported on an ultrasensitive intelligent artificial eardrum based on MXene and PDMS-PE. This artificial eardrum demonstrated an unprecedented sensitivity of 62 kPa^{-1} and a very low detection limit of 0.1 Pa. The accompanying machine-learning algorithm for real-time voice classification developed by the authors showcases a high accuracy of recognition of 96.4 and 95% [91].

The aforementioned examples of MXenes in pressure sensing applications highlight how its unique properties contribute to significant advancement in this field. High conductivity, hydrophilicity, abundance of changeable surface functional groups, customizable layer spacing and several other key characteristics of MXenes make this material particularly well-suited for pressure sensor development [92]. Most importantly, MXenes typically exhibit high electrical conductivity, which is essential for efficient signal transmission in pressure sensors. This property allows for accurate and rapid detection of pressure changes [69]. Moreover, MXenes are hydrophilic, meaning they have a strong affinity for water molecules. This property can be advantageous in pressure sensors designed to operate in humid or wet conditions as it helps maintain sensor performance in such environments [84]. MXenes’ surfaces contain an abundance of changeable functional surface groups that can be modified or altered. This provides researchers and engineers with the flexibility to tailor the surface chemistry of MXene-based pressure sensors, optimizing their sensitivity and selectivity to specific stimuli [93]. The layered structure of MXenes allows for the adjustment of interlayer spacings. Customizable layer-spacing-based tunability is valuable in pressure sensors as it enables customization to enhance the sensitivity and responsiveness to pressure variations [94].

Aerogels, hydrogels, and foams with a highly organized porous microstructure are included in the force-sensitive layers, which helps to increase the sensitivity and pressure response range. The pressure sensor’s response time and sensitivity can be increased by improving the contact between the force-sensitive layer and the electrode layer in fiber composites and fabrics made from MXenes. As a result, there is a lot of development

potential for pressure sensors based on MXenes. More examples of MXenes used in pressure sensors are presented in Table 2.

Table 2. MXene application in pressure sensors.

Composition	Sensitivity, kPa^{-1}	Test Range, kPa	LOD, Pa	Ref
MXene/CTAB/CMF	381.91	0–3	0.1	[95]
MXene/PPNs/MXene/TPUEM	34.9–177.3	0–30.4	-	[96]
MXene/Polyetherimide	20 (150 °C)–80 (–5 °C)	0–40	9	[97]
MXene/rGO/PS	115–224	0–20.65	-	[98]
MXene/bacterial cellulose (BC)	0.94–95.2	0–10	0.4	[99]

In conclusion, MXenes already play a part in the current advancements in pressure sensing technologies as they exhibit highly desired and useful qualities for sensor design including high conductivity, hydrophilicity, abundance of changeable surface functional groups, and customizable layer spacing. These inherent characteristics of MXenes contribute to its versatility in pressure sensing applications, making it a promising material for further development of advanced and high-performance pressure sensors. The inclusion of MXenes could benefit a diverse range of pressure sensors including those used in touch-screens, wearable devices, and structural health monitoring. Ongoing research is likely to further explore and optimize MXene-based pressure sensors for enhanced performance and expanded applications.

4. MXene-Based Temperature Sensors

Temperature sensors are used in various industries: from kitchen appliances to patient monitoring and reaction temperature monitoring. The sensing abilities of most temperature sensors are based on the variation in electrical properties of materials, which are sensitive to temperature. The sensing mechanisms behind MXene-based temperature and strain sensors are quite similar and are dominated by the so-called ‘crack mechanism’. Such temperature sensors consist of a temperature-sensitive substrate that expands with increasing temperature with an MXene-based layer deposited on the top. When the temperature rises, the thermal expansion of temperature-sensitive material places tensile stress on the MXene-based layer, causing it to displace and ‘crack’, which results in an increase in electrical resistance; the resistance gradually returns to its initial value when the temperature-sensitive substrate shrinks (Figure 6) [100].

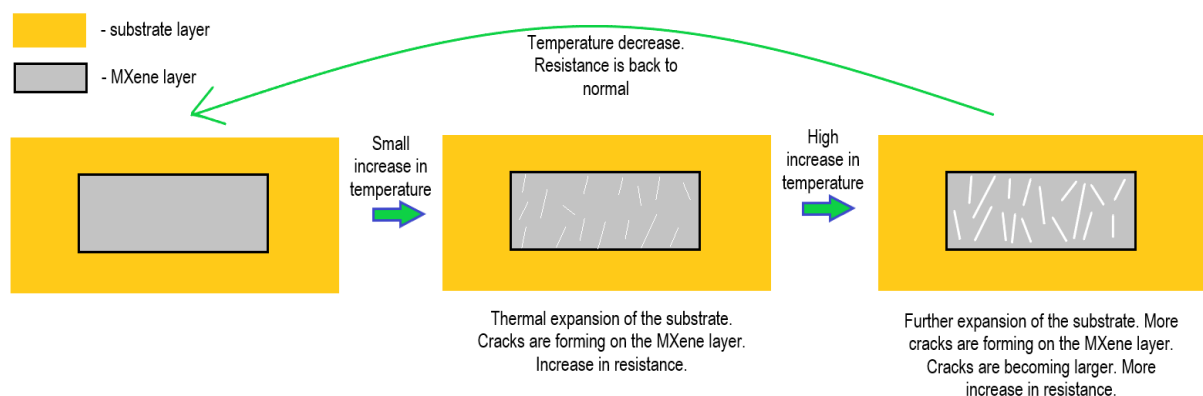


Figure 6. Crack mechanism of temperature sensors with MXenes.

Lianjia Zhao et al. developed a flexible temperature sensor using sodium alginate hydrogel as a heat-sensitive coating layer and $\text{Ti}_3\text{C}_2\text{T}_x$ MXene as a conducting skeleton. With a sensitivity up to $3244\% \text{ } ^\circ\text{C}^{-1}$, the sensor displays an accurate and consistent temperature response over the whole range (from -20 to $100 \text{ } ^\circ\text{C}$). The sensitivity of the obtained sensor

was higher compared to a metal oxide sensor, CNT sensor and PEDOT:PSS/GO sensor. It is worth noting that the linear range of the sensor was lower compared to that of the CNT sensor [101]. Zeyi Wang et al. created a $\text{Fe}^{2+}/\text{Ti}_2\text{CT}_x/\text{CA-PAM}$ hydrogel-based frost- and dehydration-resistant temperature sensor. The sensor demonstrated good linearity ($R^2 = 0.998$), sensitivity ($-1.07\% \text{ } ^\circ\text{C}^{-1}$) across a wide operating range (-10 to $60 \text{ } ^\circ\text{C}$), high resolution ($0.1 \text{ } ^\circ\text{C}$), and good repeatability. Compared to most other fire detection and warning sensor systems (based on nanoparticles, graphene oxide and metal oxides), the developed sensor demonstrated a greater reproducibility of fire detection and the benefit of the absence of a need for external power to function. The sensor's potential in health-care monitoring, electronic skins, and intelligent robotics was also demonstrated by its integration into a wireless system for body temperature monitoring [102]. By dip-coating $\text{Ti}_3\text{C}_2\text{T}_x$ MXene material on a polyester fiber substrate and depositing silver nanoparticles, Hailian Liu et al. were able to create a high-performance wearable sensor. The fiber sensor had great temperature sensitivity ($1.0436\% \text{ } ^\circ\text{C}^{-1}$ – $3.4938\% \text{ } ^\circ\text{C}^{-1}$), in addition to responding well to stimuli of temperature, pressure/strain signals [103]. $\text{Ti}_3\text{C}_2\text{T}_x$ nanoparticle–lamella hybrid networks were incorporated into PDMS substrates by Zherui Cao et al. to create a flexible temperature sensor. The sensor had a high sensitivity (up to $986\% \text{ } ^\circ\text{C}^{-1}$) and a broad response range (up to $140 \text{ } ^\circ\text{C}$), quick response time—below 7.0 s , high accuracy ($0.1 \text{ } ^\circ\text{C}$), and good dependability and durability of >100 cycles, which could meet the needs of e-skin for temperature monitoring [100]. Using graphene and $\text{Ti}_3\text{C}_2\text{T}_x$ MXene nanoinks, Mortaza Saeidi-Javash et al. presented an aerosol-based flexible bimodal sensor. The printed temperature sensor exhibited a competitive 'thermo-power' output of $53.6 \text{ V}/^\circ\text{C}$ with extremely high precision and stability. It should be noted that even after 1000 bend cycles, the printed MXene-based sensor still exhibited outstanding flexibility with barely any degradations [104].

To create a photothermal optical sensor (PHOS), Yan Zuo et al. added $\text{Ti}_3\text{C}_2\text{T}_x$ into the Mach–Zehnder interferometer (MZI) framework. An efficiency as high as $0.19 \text{ } \pi \cdot \text{mW}^{-1} \cdot \text{mm}^{-1}$ under 980 nm laser pumping was attained as a result of the $\text{Ti}_3\text{C}_2\text{T}_x$'s effective photothermal conversion, and an even higher efficiency was seen when exposed to red light. The designed scheme's response time was measured to be 23.4 s [105]. Si Chen et al. have demonstrated an all-fiber temperature sensor based on MXene V_2C . When the temperature range was ~ 25 – $70 \text{ } ^\circ\text{C}$, the corresponding transmission light intensity variation was linear, with a maximum normalized sensing efficiency of $2.21 \text{ dB} \cdot ^\circ\text{C}^{-1} \cdot \text{mm}^{-1}$. Figure 7 shows experimental setup for measuring temperature, used in the latter experiment. The runway structure used in the sensor device significantly enhanced the interaction length between light and the V_2C , thereby improving the overall sensing efficiency of the MXene-based sensor. Compared to other fiber sensors based on graphene or metal oxides, this sensor has superior sensitivity but a reduced linear range [106]. An MXene V_2C integrated runway-type micro-fiber knot resonator (MKR)-based temperature sensor was presented by Qing Wu et al. in 2023. A maximum normalized temperature sensing efficiency of $1.65 \text{ dB } ^\circ\text{C}^{-1} \cdot \text{mm}^{-1}$ was attained. The highest sensing efficiency ($\sim 0.33 \text{ dB} \cdot ^\circ\text{C}^{-1}$) was 2.7 times greater than the naked runway-type MKR's ($\sim 0.09 \text{ dB} \cdot ^\circ\text{C}^{-1}$) [107].

MXene-based temperature sensors encounter specific challenges that warrant attention. Firstly, despite exhibiting superior qualities compared to some alternative materials, MXene-based sensors face accuracy issues when utilized for temperature measurements. Secondly, the current manufacturing methods for temperature sensors, which often involve distinct processing steps and intricate fabrication designs, may compromise the comfort of wearable devices. Overcoming these challenges is crucial for optimizing the performance and applicability of MXene-based temperature sensors in various applications [108]. In general, compared to other materials, MXenes usually provide advanced sensitivity but lower stability and smaller linear range.

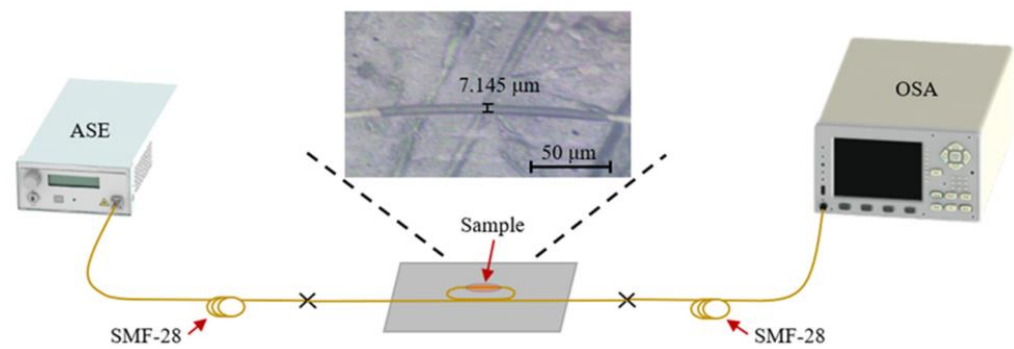


Figure 7. Experimental setup for temperature sensing. Reprinted from [106].

5. MXene-Based Humidity Sensors

Monitoring and regulating humidity have become increasingly crucial in various industries, such as agriculture, textile technology, and food storage. The significance of controlling humidity levels stems from its direct impact on product quality, preservation, and overall operational efficiency within these sectors. As a result, precise humidity management is now integral to maintaining optimal conditions for crop growth, ensuring the quality of textiles, and preserving the freshness and safety of food products during storage and transportation. The evolving importance of humidity control underscores its pivotal role in enhancing performance and outcomes across diverse industrial applications [109–111]. For these applications, it is crucial to detect relative humidity (RH) with good accuracy, sensitivity, and reliability. $\text{Ti}_3\text{C}_2\text{T}_x$ MXene possesses terminal groups that provide ample hydrophilic active sites for water adsorption and intercalation [112,113], in contrast to semiconductor metal oxides where water-molecule-dependent surface conductivity dominates the sensing mechanism [114,115]. The low electrical conductivity of water and the lengthening of the layer-to-layer distance will result in an increase in $\text{Ti}_3\text{C}_2\text{T}_x$ resistance following the intercalation of water molecules in the interlayers between 2D MXene sheets [113,116]. Thus, $\text{Ti}_3\text{C}_2\text{T}_x$ MXene provides a sensing mechanism that is suitable for RH sensing [117].

Layer-by-layer assembly was used by Hyosung An et al. to create MXene/polyelectrolyte (poly(diallyldimethylammonium chloride)) multilayer films, which displayed extremely quick response (110 ms) and recovery (220 ms) times in the RH range of 20–40%. The sensor was successfully employed to monitor human respiration in real time, though the authors noted that direct contact with the electrolyte can lead to skin irritation. It was also shown how increasing the space between sheets increased the tunable resistance by intercalating water molecules into multilayers [118]. Yang Lu et al. described the fabrication of an impedance-type humidity sensor based on $\text{Ti}_3\text{C}_2\text{T}_x/\text{g-C}_3\text{N}_4$ nanomaterials. They investigated the process of humidity sensing using complex impedance spectroscopy, finding that the major conductive ion is H_3O^+ at RH between 11% and 43%. Physisorbed water layers began to grow on top of the initial chemisorbed water layer as the Grotthuss chain reaction ($\text{H}_2\text{O} + \text{H}_3\text{O}^+ \rightarrow \text{H}_3\text{O}^+ + \text{H}_2\text{O}$) governed charge transportation at this stage, where the major charge carriers H^+ move freely. As a result, the impedance dropped as the humidity increased, which formed the groundwork for the created sensor. At a range of 11–97% RH, the humidity sensor demonstrated exceptional repeatability, fast response and recovery times (4.8 and 8.9 s, respectively), and neglectable hysteresis. The response was significantly stronger than that of most other impedimetric sensors based on other materials (namely, Ag or LiCl). The authors showed how it might be used to detect water evaporation and monitor human breath [119]. Mimi Han et al. assembled MXene nanosheets into a layered TOCNF/MXene nanocomposite film utilizing vacuum-assisted filtration and (TEMPO)-oxidized cellulose nanofibers (TOCNFs) as a template. The swelling and contraction of channels between MXene interlayers caused by adsorbed H_2O and the swelling of TOCNFs were both components of the sensor's humidity-sensing mechanism. The TOCNF/MXene sensor displayed exceptional bending and folding durability (up to

50 cycles), long-term stability, and a maximum response ($-\Delta I/I_0$) of 90% under 97% RH. The authors demonstrated the sensor applications in smart wearable electronics by dynamically monitoring human breath, skin, and fingertip humidity [120].

By fluoride doping, Runlong Li et al. improved the MXene quartz crystal microbalance-based humidity sensor. They demonstrated that the resulting sensor had 12.8 Hz/% RH sensitivity compared to 10.2% for the fluoride-free sensor that was made using the same procedure. The fluoride-doped sensor showed a rapid response time of 6 s and 2 s, a maximum humidity hysteresis of 1.16% RH, high short-term repeatability, long-term stability, and excellent selectivity in the range of 11.3–97.3% RH [121]. In 2017, Eric S. Muckley and colleagues developed a material for humidity detection by intercalating K and Mg between the MXene layers. They were able to demonstrate that the d-spacing was initially larger for $\text{Ti}_3\text{C}_2\text{-K}$ (11.5 Å versus 10.1 Å in $\text{Ti}_3\text{C}_2\text{-Mg}$) using neutron scattering. After hydration, $\text{Ti}_3\text{C}_2\text{-Mg}$ had a greater d-spacing (14.6 Å against 12.4 Å in $\text{Ti}_3\text{C}_2\text{-K}$) as the smaller size and higher charge of Mg^{2+} allow for a stronger interaction with H_2O , resulting in a larger hydrated radius of Mg^{2+} (~4.28 Å versus ~3.31 Å). The greater radius causes a bigger hydrated d-spacing in $\text{Ti}_3\text{C}_2\text{-Mg}$ after hydration. The emerged $\text{Mg}(\text{H}_2\text{O})_6$ cluster was shown to be the best candidate for the pillaring effect as a result of creating a stiff structure. Relative humidity (RH) detection thresholds of ~0.8% RH were found in $\text{Ti}_3\text{C}_2\text{-K}$ and $\text{Ti}_3\text{C}_2\text{-Mg}$ films, and they also demonstrated a monotonic RH response in the 0–85% RH range with ~3% resolution [122].

One of the other methods of improving sensitivity is alkaline treatment. Organ-like alkalinized $\text{Ti}_3\text{C}_2\text{T}_x$ sensors were created by Zijie Yang et al. to monitor NH_3 and humidity at room temperature. The device based on alkalinized $\text{Ti}_3\text{C}_2\text{T}_x$ had opposite response signals with improved NH_3 and humidity detecting capabilities compared to not alkalinized $\text{Ti}_3\text{C}_2\text{T}_x$. The $\text{Ti}_3\text{C}_2\text{T}_x$ altered carrier type of conductivity following oxygen functionalization was the cause of the response signal's change in direction [16].

6. MXene-Based Gas Sensors

The fast industrialization of society has created numerous issues related to volatile pollutants and greenhouse gases, posing threats to both the environment and human health. Detecting and quantifying the presence of harmful gases in a timely and precise manner are essential both for mitigating the negative effects of the pollutants and for providing accurate data for environmental research. MXenes are currently attracting significant attention in the field of gas sensing due to their exceptional qualities, such as their high metallic conductivity, abundant and tunable functional groups (-OH, -O, or -F), porous structure, and quick electron transfer ability [123,124].

The fundamental gas sensing process of pure MXenes' is based on the adsorption and desorption of gas from the sensing layer and the ensuing change in the concentration of free charge carriers [125]. The alteration in the electrical conductivity of MXenes arises from the reaction of target gases (as demonstrated in Figure 8 for NH_3) with surface defects and termination groups:

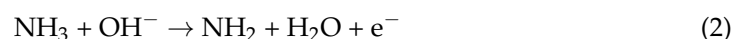
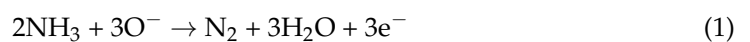


Figure 8 show General gas sensing mechanism of pristine MXenes for NH_3 .

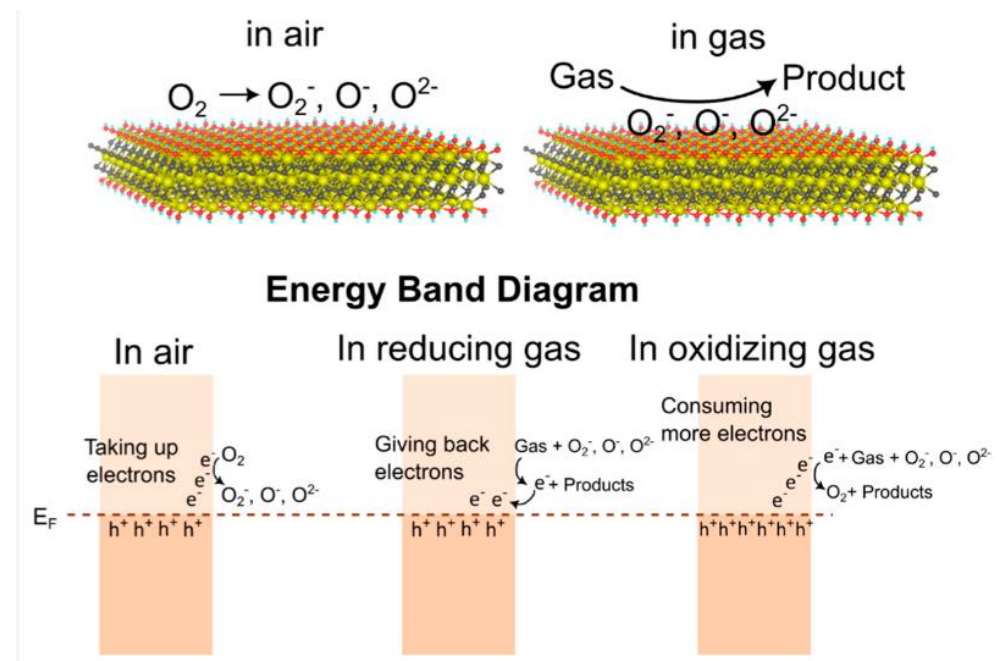


Figure 8. Gas sensing mechanism of the pristine 2D MXenes and the corresponding energy band diagram. Reprinted from [126].

Despite their unique properties, pristine bare MXenes face certain limitations that hinder their effectiveness as sensing materials sensitive towards a broad range of gases. Challenges during the development of gas sensors include a lack of specificity to certain gas groups (excluding hydrogen-binding gases like acetone and NH_3 as research shows MXenes have high selectivity towards it, compared to most other 2D materials [127,128]) and molecular structures, a relatively low bandgap, and a mechanical stability that is not always sufficient. These limitations can impact the sensitivity and selectivity of MXene-based gas sensors, making them less suitable for comprehensive gas sensing applications. Researchers and engineers are actively exploring various strategies to overcome these challenges. Surface functionalization, hybridization with other materials, and structural modifications are some of the approaches being investigated to enhance the performance and detection spectrum of MXene-based gas sensors [129,130]. Synergistic approaches with other materials, such as metal oxides, conducting or non-conducting polymers, 2D carbon nanomaterials, chalcogenides, and other surface functionalizing materials, might improve the properties of pure MXene sensors [16,122]. Depending on the characteristics of the components, the synergistic and reverse enhancing effect in MXene composites directly affects the sensing mechanism. For example, the basic mechanism for MXene composites containing metal oxides is quite similar to that of conventional metal oxide semiconductor-based sensors, in which the gas analyte's effective absorption or desorption on the surface of the sensing material results in a change in the device's resistance. The interfacial interactions between the two contributing materials and heterojunction production are related to the gas-sensing process of MXene-metal oxide composites [131].

6.1. NH_3 Sensing by MXene-Based Sensors

Ammonia (NH_3) is an important raw material in many domains. However, NH_3 is a hazardous, corrosive, and colorless odor gas, and even at low concentrations can be dangerous to human health [132–134]. Therefore, quick and accurate monitoring of NH_3 gas is crucial to ensure safety in industrial settings [135]. Xiao and co-workers revealed the advantages of using MXenes for NH_3 sensing using first-principle simulation. The results showed that NH_3 has a strong affinity to MXene substrates [136].

Seon Joon Kim and colleagues used interfacial self-assembly to create ultrathin Ti_3C_2 MXene films. The film was able to detect a concentration of 5 ppm NH_3 , and its sensitivity was 0.46% [137]. Eunji Lee et al. assembled $\text{Ti}_3\text{C}_2\text{T}_x$ MXene sheets on flexible polyimide platforms using a straightforward solution-based technique. The constructed sensors responded strongly to ammonia (100 ppm with a sensitivity of 0.21%) [127]. Meng Wu et al. created Ti_3C_2 MXene-based sensors that had a varying-resistance-based response to numerous gases, namely CH_4 , H_2S , methanol, ethanol, acetone, NH_3 , and NO . The sensors had good selectivity for NH_3 , with a 6.13% response, LOD of 10 ppm, and good linearity in the 10–700 ppm range [128].

Despite promising results, low sensitivity, long recovery time, and resistance drift after exposure to NH_3 are still major issues for room temperature sensing of NH_3 using pristine $\text{Ti}_3\text{C}_2\text{T}_x$ MXene sensors [16,127,128]. Additional nanomaterials like graphene, carbon nanotubes (CNTs), reduced graphene oxide (rGO), and graphene oxide (GO) can be applied to promote the reaction with NH_3 gas molecule [138]. By using a scalable wet-spinning technique, Sang Hoon Lee et al. created $\text{Ti}_3\text{C}_2\text{T}_x$ MXene/graphene hybrid fibers. Excellent mechanical and electrical qualities made these fibers ideal for use in flexible wearable gas sensors. According to the authors, in comparison to pure MXene and graphene, the NH_3 sensing response was considerably improved ($\Delta R/R_0 = 6.77\%$) in the created sensor [129].

Metal oxides are frequently chosen as sensing film materials for various sensing devices [139,140]. Metal oxides are also applied to further improve the NH_3 sensing properties of resistive-based gas sensors because they can prepare a high amount of charge carriers [138]. TiO_2 - [141], nonstoichiometric- TiO_2 - [142,143] and WO_3 -based [144–146] gas sensors are very promising for NH_3 detection. $\text{In}_2\text{O}_3/\text{Ti}_3\text{C}_2\text{T}_x$ MXene composites were created by Miao Liu et al. and displayed exceptional gas sensing qualities, including a high response (60.6%) to 5 ppm NH_3 at RT, rapid response/recovery time (3/2 s), excellent selectivity, linearity, and good stability in the 5–100 ppm range. Compared to pristine MXene sensors and other metal oxides sensors, the designed sensor had better sensitivity and higher response to NH_3 [147]. A hybrid heterojunction structure was created by Miao Liu et al. using the $\alpha\text{-Fe}_2\text{O}_3/\text{Ti}_3\text{C}_2\text{T}_x$ MXene composite material, which has a high specific surface area and a lot of functional groups. For 5 ppm NH_3 , the $\text{Fe}_2\text{O}_3/\text{Ti}_3\text{C}_2\text{T}_x$ MXene sensor showed a response value of 18.3% and quick response/recovery times sub 2.5 s [135]. A ZnO/MXene hybrid surface acoustic wave (SAW) sensor was designed by Kedhareswara Sairam Pasupuleti et al. The sensor increased selectivity with an ultralow detection limit (89.41 ppb), displayed quick response/recovery time (92/104 s), long-term stability, and strong sensitivity under UV activation [148]. To improve the NH_3 sensing capabilities of $\alpha\text{-Fe}_2\text{O}_3$, Miao Liu et al. created a hybrid structure of three components: Au, $\alpha\text{-Fe}_2\text{O}_3$, and $\text{Ti}_3\text{C}_2\text{T}_x$ MXene. The $\text{Au}/\alpha\text{-Fe}_2\text{O}_3/\text{Ti}_3\text{C}_2\text{T}_x$ MXene sensor displayed an excellent NH_3 sensing performance, and its response value to NH_3 (1 ppm) reached 16.9% at RT. Compared to other sensors (based on pure MXene or metal oxides), the obtained sensor had better sensitivity and response/recovery times [149].

The need for wearable NH_3 sensors capable of real-time monitoring on diverse surfaces, including skin and clothing, is rather urgent. Polymer-based sensors have gained attention as one of the most promising options for addressing this requirement [150]. Polymer materials offer versatility and compatibility with a variety of substrates [151], making them well-suited for wearable sensor applications [152,153]. Polymer-based sensors can be designed to be flexible, lightweight, and adaptable, allowing for comfortable integration into wearable devices [140,154]. Additionally, polymers can exhibit sensitivity to specific gases, including NH_3 , and their properties can be tailored to enhance selectivity and performance [155,156]. The development of wearable NH_3 sensors using polymer materials holds great potential for applications in various fields, including agriculture, environmental monitoring, and personal health. Ongoing research aims to optimize the design and performance of these sensors, paving the way for effective and versatile real-time monitoring solutions [157]. PEDOT:PSS/MXene composites were made by Ling Jin et al. and used in the fabrication of a dip-coated gas sensor. The composite sensor demonstrated a gas re-

sponse of 36.6% against 100 ppm of NH_3 , with the response and recovery times being 116 s and 40 s, respectively. Additionally, it showed superior NH_3 sensing performance at RT compared to pure PEDOT:PSS- and MXene-based sensors [158]. A portable self-powered NH_3 sensor device was designed by Xingwei Wang et al. by implementing a bi-functional material made of 2D PANI/ V_2C MXene nanosheets. The authors discovered that the PANI/ V_2C nanosheets perform much better than pure PANI and MXene nanosheets in terms of response value ($\Delta R/R_0 = 14.9\%$), stability, and response/recovery time (9 s and 9 s) [159]. $\text{Zr}_3\text{C}_2\text{O}_2$ -based MXene is also a suitable material for room temperature NH_3 sensors with excellent sensitivity and great selectivity, according to Xiumei Li et al. They proposed that a monolayer of $\text{Zr}_3\text{C}_2\text{O}_2$ can be used as an NH_3 detector since the NH_3 molecule can be weakly chemically adsorbed with an adsorption energy of -0.597 eV, noticeable charge transfers (0.117 e), and a quick recovery time (1.05 ms) [160]. Such weak adsorption is a technological advantage because it enables easy and fast regeneration of the sensor. In conclusion, the discussed research results for MXene-based ammonia sensors showcase impressive applicability and potential for further development.

6.2. Determination of Volatile Organic Compounds (VOCs)

A wide range of sectors, including industrial safety control, environmental monitoring, and personal health management, have benefited greatly from the invention of gas sensors that are capable of accurately detecting volatile organic compounds (VOCs). These sensors play a crucial role in ensuring safety in industrial settings by monitoring the concentrations of VOCs and provide the necessary tools for environmental monitoring such as air quality evaluation. As VOC exposure can negatively impact personal health, sensors integrated into personal devices or wearable technology and able to provide real-time information about the surrounding air could ensure that the users are informed about the possible dangers of the environment they are in. Additionally, detection of VOCs emitted from the individual's breath can also aid in early detection of certain illnesses and provide various health insights. Moreover, such sensors would be beneficial in residential and commercial spaces to monitor the indoor air quality and help in maintaining a comfortable and safe environment for the users of the space. Due to the abovementioned reasons, rapid advancements in VOC sensor technologies are important to our society as they contribute to improved safety, environmental sustainability, and overall human well-being in various areas [161–163]. Acetone sensors are gaining popularity due to their promising uses in self-diagnosis and health monitoring [164,165]. As an example, the acetone concentration in human breath is recognized as a crucial indicator for the identification of diabetes [166]. $\text{W}_{18}\text{O}_{49}/\text{Ti}_3\text{C}_2\text{T}_x$ composites were made by Shibin Sun et al. by combining $\text{Ti}_3\text{C}_2\text{T}_x$ MXene sheets with $\text{W}_{18}\text{O}_{49}$ nanorods. The obtained $\text{W}_{18}\text{O}_{49}/\text{Ti}_3\text{C}_2\text{T}_x$ -based acetone sensor exhibited an extremely low detection limit of 170 ppb, a quick response/recovery times (5.6/6 s to 170 ppb of acetone), and a high response of 11.6 to 20 ppm of acetone. The sensor also demonstrated nearly ideal selectivity towards acetone. However, the main problem with this parameter was the high response to ammonia, though authors claim that due to slower response and recovery rates to NH_3 , this should not be an issue. According to the authors, the distribution of $\text{W}_{18}\text{O}_{49}$ on the $\text{Ti}_3\text{C}_2\text{T}_x$ surface, the removal of the fluorine terminational groups from the MXene, and the synergistic interactions between the $\text{W}_{18}\text{O}_{49}$ and the $\text{Ti}_3\text{C}_2\text{T}_x$ provided the combined sensors superior acetone-sensing properties in comparison to $\text{W}_{18}\text{O}_{49}$ and $\text{Ti}_3\text{C}_2\text{T}_x$ sensors [167]. The 3D $\text{Ti}_3\text{C}_2\text{T}_x$ MXene/rGO/CuO aerogel sensor developed by Miao Liu et al. responded to 100 ppm acetone with a 52.09% rate at room temperature and demonstrated a quick response/recovery time (6.5 s/7.5 s) as well as high repeatability and selectivity. According to the scientists, the results are due to the highly interconnected porous structure and the combined effects of MXene, rGO, and CuO. Compared to pristine MXene and rGO/ In_2O_3 sensors, the obtained sensor had a superior response/recovery time and higher response [168]. An urchin-like $\text{V}_2\text{CT}_x/\text{V}_2\text{O}_5$ MXene hybrid sensor was developed by Sanjit Manohar Majhi et al., and it demonstrated an increased response ($S\% = 11.9$) toward 15 ppm acetone, a low limit of detection (250 ppb), and

a quick response/recovery time (115s/180s). The selectivity test showed higher response to acetone in comparison to CO, H₂, CO₂, H₂S and C₂H₄ (47% versus <15% towards other gases). According to the authors, the potential production of H-bonds in multilayer V₂C MXenes, the synergistic effect of the created V₂C/V₂O₅ composite, and the strong charge carrier transport at the V₂O₅ and V₂C MXene interface can be applied for improving the sensing properties [169].

Gaseous toluene (C₆H₅CH₃) is a dangerous VOC that is created during the process of tanning leather and other materials. Even at rather low concentrations, it is deadly to humans and very harmful to the environment [170,171]. To decrease the risk to one's health from exposure to toluene gas, it is crucial to detect it early and monitor its concentration both indoors and outdoors. CuO/Ti₃C₂T_x MXene hybrids were created by Angga Hermawan et al., who also attributed the increased toluene gas sensing response of 11.4, selectivity, response (270 s) and recovery times (10 s) to the strong metallic phase conductivity of Ti₃C₂T_x. However, the developed sensor had some significant issues with selectivity. The response signal to toluene was not much higher compared to ethanol and acetone signals (~11% versus 7%, respectively) [172]. A toluene sensor based on the MXene Mo₂CT_x was proposed by Wenzhe Guo et al. It had an LOD of 220 ppb, an adequate selectivity for toluene against other VOCs (2.75% response compared to 1% of benzene and even lower responses towards other analytes), and a good sensitivity of 0.0366 Ω/ppm (140 ppm for toluene) [173].

Formaldehyde (HCHO) has been regarded as the primary contributor to sick building syndrome [174,175]. HCHO can cause the irritation of mucous membranes, skin, eyes and throat, cause shortness of breath, headaches, nausea, and possibly lead to cancer. This substance is one of the most harmful and carcinogenic VOC gases in urban and indoor environments [176–178]. Therefore, it has become necessary to create high-performance portable HCHO sensors. Co₃O₄ and ZnO/Ti₃C₂T_x MXene nanowire arrays were used to create the composite-based formaldehyde sensor that was proposed by Dongzhi Zhang and colleagues. The MXene/Co₃O₄ composite sensor demonstrated selectivity (~9.5% compared to the highest of ~1.75% towards acetone) and outstanding response characteristics (9.2 to 10 ppm HCHO, with an LOD of 0.01 ppm). The selectivity to HCHO was also improved compared to pure MXene and Co₃O₄ sensors. The synergistic interfacial interactions between MXene and Co₃O₄ were thought to be the cause of the improved responsiveness to HCHO [179]. To design a formaldehyde sensor, Gaoqiang Niu et al. applied a pre-oxidation technique to change SnO₂/Ti₃C₂T_x MXene into SnO₂/TiO₂/Ti₃C₂T_x MXene nanocomposites. Due to the synergistic interaction between SnO₂ nanosheets and TiO₂/Ti₃C₂T_x MXene, the sensor demonstrated a high response rate (38.6 at 160 °C to 20 ppm with LOD being 50 ppb), strong selectivity (38.4 compared to the highest 16.0 towards ethanol), and reproducibility. When the selectivity of the sensor was compared to a pure SnO₂ sensor, the results showed clear improvement of the signal (38.4 compared to <20%) [180].

Another VOC, methanol, is used as an organic solvent in numerous sectors, including the pharmaceutical, chemical, biomedical, and automotive industries. However, it is extremely combustible and has a low explosive limit of 6% in air. When a person is exposed to more than 200 ppm of methanol for 8 h, it can lead to intoxication [181]. Additionally, unlike other alcohols, methanol oxidizes slowly and builds up in the human body, which can result in poisoning. Therefore, it is crucial to design a methanol sensor that has good sensitivity and selectivity and can operate at ambient temperatures [182]. In₂O₃ nanocubes/Ti₃C₂T_x MXene nanocomposites showed strong responsiveness (29.6% to 5 ppm) and noticeable selectivity to methanol against other gases (30% towards methanol versus <18% towards trimethylamine, acetone, xylene and other gases) at room temperature, as reported by Miao Liu et al. According to the authors, the sensor was characterized by quick reaction and recovery times (6.5 and 3.5 s, respectively) to 5 ppm methanol at ambient temperature [183].

Ethanol is employed extensively in the pharmaceutical, food manufacturing, and biomedical industries as a key chemical ingredient [184,185]. Ethanol also poses a serious risk to the safety of production and transportation due to its combustible and explosive nature (explosion range of 3.3% to 19%) [186]. Additionally, long-term exposure to an atmosphere even with low levels of ethanol (25 ppm) can lead to serious negative health effects, including headaches, liver damage, and neurasthenia [187,188]. Therefore, designing and creating sensing materials for monitoring low-concentration ethanol gas at low temperatures is greatly important. Shuai Zhang et al. developed $\text{MoO}_3/\text{Ti}_3\text{C}_2\text{T}_x$ MXene nanocomposites employing a straightforward hydrothermal synthesis technique for efficient monitoring of low ethanol concentrations. The sensor responded well to low-concentration ethanol gas at 100 °C ($R_a/R_g = 1.61/1$ ppm) and recovered quickly (10 s/49 s). Outstanding selectivity for ethanol was obtained, with the response being five times higher compared to other gases, like methanol and acetone [189]. In order to create resistance-type gas sensors, Chen Wang et al. produced $\text{SnO}_2/\text{MXene}$ composites that were brushed onto a MEMS platform. The composition significantly increased the sensitivity of SnO_2 -based gas sensor, with ethanol gas having the maximum sensitivity. The composite additionally accelerated the sensor's response and recovery times (14s and 26s, respectively) and reached a 5.0 response value to 10 ppm ethanol at its ideal temperature of 230 °C, which was twice as high as the response value of a pure SnO_2 sensor. Though the selectivity of the sensor was improved after adding MXenes, the response towards acetone is still comparable to ethanol (~4 towards acetone compared to ~5 towards ethanol). The improvement in the composite's gas-sensing characteristics is attributed, according to the authors, to its Schottky barrier and the metal-like conductivity of $\text{Ti}_3\text{C}_2\text{T}_x$ [190].

6.3. Other Gas Sensors Based on MXenes

There are other gases that can be monitored by MXene-based gas sensors. One of them is H_2 , a gas with a significant energy capacity that is renewable and sustainable. It is commonly used in the metallurgy, fuel cell, and automotive industries [191,192]. However, H_2 gas is highly explosive in air at concentrations of more than 4% and has a low ignition energy. Additionally, due to its small molecule size and high diffusion coefficient, it leaks during usage, storage, and transit [193,194]. Because H_2 gas is odorless, our sense of smell system is unable to detect it; hence, the creation of high-response H_2 sensors is essential to guaranty safety. A unique Pt = Pd/ $\text{Ti}_3\text{C}_2\text{T}_x$ hydrogen sensor was developed by Lei Wang et al. using a simple hydrothermal chemical reduction process. The resulting sensor had a response of 24.6% (200 ppm H_2 at RT), a response/recovery time of 6/8 s, an LOD of 200 ppm, and strong selectivity (24.6% for hydrogen compared to the highest towards ethanol 5.2%) in addition to good linearity, long-term stability, and repeatability [195].

The main sources of nitrogen dioxide (NO_2) are industrial combustion, automotive exhaust, and coal mining. According to research, even very small concentrations of NO_2 (~1 ppm) can harm the respiratory system and eyes to varying degrees. Furthermore, persistent exposure to higher NO_2 concentrations may possibly be fatal to humans [196]. Fuqiang Guo et al. effectively created $\text{Ti}_3\text{C}_2\text{T}_x/\text{CuO}$ nanocomposites using an eco-friendly and straightforward hydrothermal process for NO_2 sensing. The response of the author's nanocomposite sensor to NO_2 (56.99%) was five times greater than that of the pure $\text{Ti}_3\text{C}_2\text{T}_x$ sensor. The improved gas sensing capability was attributed to higher oxygen vacancies and adsorbed oxygen in comparison to $\text{Ti}_3\text{C}_2\text{T}_x$ as well as hybrid heterojunctions between CuO and $\text{Ti}_3\text{C}_2\text{T}_x$. The $\text{Ti}_3\text{C}_2\text{T}_x/\text{CuO}$ sensor demonstrated extremely quick response and recovery times (16.6/31.3 s to 20 ppm NO_2), exceptional selectivity to NO_2 (with the response being ~57% towards NO_2 versus 31.09% towards NO and 12.63% towards ammonia), and long-term stability [197].

Other researchers have demonstrated that other gases, such as NO_x [198,199], hexanal [200] and others [201,202], can also be determined by gas sensors based on MXenes. It can be predicted that due to the unique characteristics of MXenes, such as tunable terminal groups, and metallic conductivity, they have been successfully applied in gas sensor design.

Compared to other materials, pristine MXenes can offer high sensitivity with mediocre selectivity (except for hydrogen bonding gases) and a lower linear range. Combining MXenes with other more selective or more stable materials (especially with metal oxides or metal nanoparticles) usually results in much better results.

7. Chemical Sensors

The socio-economic changes induced by industrialization in the middle of the 19th and 20th centuries have considerably improved the quality of life of many people. However, such advancements have also resulted in pollution and contamination of water, soil, air, etc. Naturally, MXene nanomaterials have drawn a lot of interest in the field of pesticide sensing, heavy metal sensing, etc., because of their exceptional electrical and optical properties. Efficient functionalization of MXenes is made possible by the surface termination groups, which is essential for electrochemical sensing [203] as they give MXenes a superb reducing ability. Qualities of MXenes make them suitable for improvement of the functionality of sensors and biosensors, providing higher sensitivity, selectivity to some analytes, and strong reproducibility but shorter detection ranges compared to other materials. Though MXenes have remarkable electrocatalytic activity, one of their main flaws is that they are unstable in the anodic potential window and exhibit an irreversible oxidation peak at roughly 0.43 V. Thus, combining MXenes with other components is essential for further enhancement of sensory abilities [204].

7.1. Nitrite Sensors

Nitrite (NO_2^-) is one of the most prevalent nitrogen-containing ions, which is widely used in the chemical and food industries [205,206]. Detection of nitrite is important as it poses serious dangers for human health. The nitrite oxidizes hemoglobin into methemoglobin, reducing the blood's ability to carry oxygen [207], and it can also react to form N-nitrosamine, which can cause stomach cancer [208]. Tan Wang et al. created a novel nanocomposite of AuNPs/ $\text{Ti}_3\text{C}_2\text{T}_x$ /ERGO for the sensitive electrochemical detection of nitrite. AuNPs/MXene/ERGO exhibited enhanced catalysis for nitrite oxidation compared to ERGO, MXENE/ERGO, and AuNPs/ERGO due to the synergy of these components. The developed sensor's overall electrocatalytic oxidation of nitrite followed the mechanism:

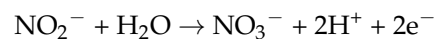
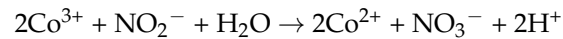
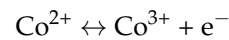


Figure 9 shows the detection scheme using the obtained sensor. Linear ranges of obtained sensors were 0.5 to 80 μM and 80 to 780 μM , respectively, with an LOD of 0.15 μM and 0.015 μM and a sensitivity of 340.14 and 977.89 $\mu\text{A}\cdot\text{mM}^{-1}\text{cm}^{-2}$ with great selectivity to nitrite (the sensor did not react to different interference salts, like KCl and NaNO_3 , even when their concentrations were much higher) [209].

The synergetic catalytic effect of the AuNPs/ $\text{Ti}_3\text{C}_2\text{T}_x$ -PDDA nitrite sensor was designed by Yuhuan Wang et al. The $\text{Ti}_3\text{C}_2\text{T}_x$ improved electron transport, and $\text{Ti}_3\text{C}_2\text{T}_x$ -PDDA composites gave AuNPs more places to attach during the electrodeposition process. The AuNPs/ $\text{Ti}_3\text{C}_2\text{T}_x$ -PDDA/GCE sensor demonstrated exceptional linear ranges in the ranges of 0.1–2490 μM and 2490–13490 μM , high sensitivity of 250 $\mu\text{A}\cdot\text{mM}^{-1}\cdot\text{cm}^{-2}$, and great selectivity with an LOD of 0.059 μM . The sensor had a superior working range length and detection limit compared to a combination of AuNPs with graphene or CNT [210]. In order to combine the great electrocatalytic activity of AuNPs with carbon quantum dots (CQDs), MXene's substantial specific surface area, and the good electrical conductivity of AuNPs with MXene, Xiwen Feng et al. created a AuNPs@CQDs- $\text{Ti}_3\text{C}_2\text{T}_x$ MXene nitrite sensor, where MXene was used as the immobilization matrix. The sensor had a detection limit of 0.078 μM and a linear detection range of 1 μM to 3200 μM with great sensitivity and selectivity, as the sensor did not respond towards nitrates, chlorides and sulphates. However, it is worth noting that working range and detection limit were inferior to the AuNPs/ $\text{Ti}_3\text{C}_2\text{T}_x$ -PDDA sensor [211]. A novel electrochemical sensing platform for nitrite detection was developed by Jinghao Zhuang et al. It was based on a $\text{Ti}_3\text{C}_2\text{T}_x$ MXene sheet

and a three-dimensional urchin-like $\text{Co}(\text{VO}_3)_2(\text{H}_2\text{O})_4$ (CoVO). The following was proposed as the mechanism for the electrochemical reduction of nitrite on CoVO/ $\text{Ti}_3\text{C}_2\text{T}_x$ electrodes:



The CoVO/ $\text{Ti}_3\text{C}_2\text{T}_x$ -based composite displayed a significantly improved electrochemical signal with good linearity in the range of 0.5–50 μM and 50–2000 μM with an LOD of 0.1 μM [212].

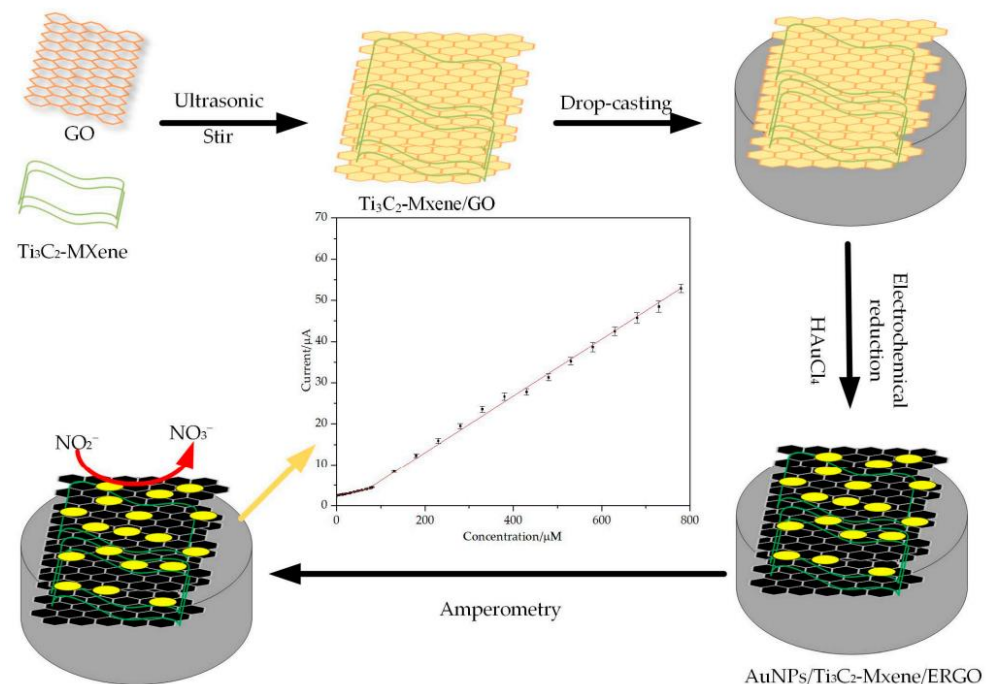
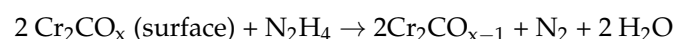


Figure 9. Nitrite detection scheme of AuNPs/MXene/ERGO-based sensor. Reprinted from [209].

7.2. Hydrazine Sensors

Hydrazine and its derivatives are widely used in fuel cells, photography, insecticides, dyes, and pharmaceuticals [213]. Hydrazine is a known carcinogen and exposure to it can cause temporary blindness, skin allergies, carcinogenesis, neurotoxicity, and organ damage, especially to the liver and kidneys [214]. Additionally, industrial waste and waterways contain it, making it a potentially widespread environmental pollutant [213]. Therefore, creating efficient methods to detect hydrazine at low concentrations is essential from an industrial, medical, and environmental perspective. The idea of using few-layered (FL) Cr_2CT_x MXene nanosheets as a receptor integrated into a microresonator to detect hydrazine at the ppm level was proposed by Bhuvaneshwari Soundiraraju et al. [215]. The same author designed a FL- Cr_2CT_x modified electrode for hydrazine detection. With an LOD of 6.60×10^{-7} M (at S/N = 3), the electrode demonstrated a high sensitivity of $1.810 \mu\text{A} \cdot \mu\text{M}^{-1}$ towards hydrazine. The LOD for hydrazine was also more than 10 times lower than that achieved by electrodes modified by $\text{Ti}_3\text{C}_2\text{T}_x$ and Nb_2CT_x -based pristine MXenes. The authors also presented a possible mechanism for detecting hydrazine by the sensor:

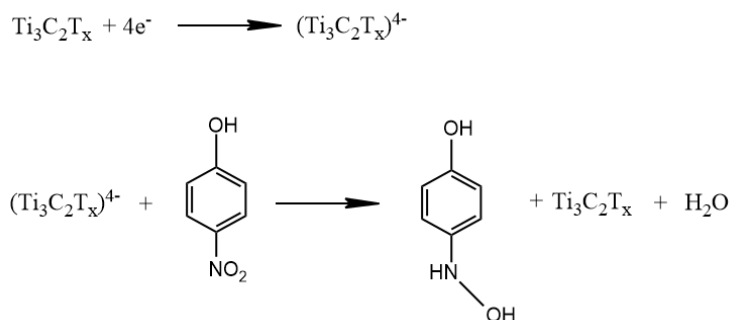


The developed sensor was also employed to quantitatively analyze hydrazine liquid propellant spiked in water with satisfying results [216]. Yanqing Yao et al. intercalated a $\text{Ti}_3\text{C}_2\text{T}_x$ -based MXene as a conductive platform, which dramatically increased the con-

ductivity of ZIF-8. The obtained sensor demonstrated excellent sensing performance for hydrazine, with amazing selectivity (with no reaction to nitrates, chlorides, ethanol, DMF and other possible interferences), a 10–7700 μM linear range, and an LOD of 5.1 μM , thanks to the synergistic effect of MXene/ZIF-8 nanocomposite. Compared to other sensors, the MXene/ZIF-8 sensor had a superior linear range, but it lacked a sufficient LOD [217]. Sundus Gul et al. used Nb_2C MXene as a direct electrode material for electrochemical hydrazine sensing. They also added erbium (Er) to several Nb_2C MXene samples and compared the results with non-doped ones. The pure MXene and Er-doped samples were found to have sensitivity values of $169 \mu\text{A}\cdot\text{M}^{-1}\cdot\text{cm}^{-2}$ and $276 \mu\text{A}\cdot\text{M}^{-1}\cdot\text{cm}^{-2}$ and LOD values of 10.08 mM and 67 μM , respectively, demonstrating that the Er-doped MXene is significantly more sensitive than the unmodified one. According to the authors both mentioned MXenes are potential candidates for hydrazine sensing [218].

7.3. Sensing of Phenol and Its Derivatives

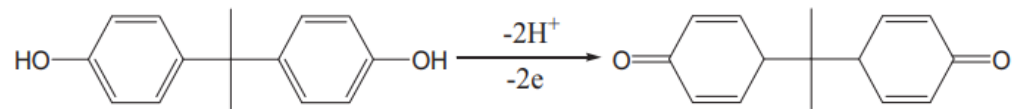
The US Environmental Protection Agency and the European Union have identified phenolic compounds as environmental contaminants [219]. Phenolic compounds are common waste products of many chemical facilities. Bisphenols are frequently employed in a range of industries, along with benzenediols and aminophenols. Many of these compounds, even in very low quantities, are harmful to people, plants, animals, and biological and ecological ecosystems [220]. Thus, developing sensors to monitor the aforementioned substances is important to ensure the health of society and the environment. Lingxia Wu et al. described the application of Ti_3C_2 in phenol sensing [221]. According to Ling Lei et al., $\text{Ti}_3\text{C}_2\text{T}_x$ MXene nanosheets are significantly more active for the oxidation of 4-chlorophenol (4-CP) and 4-nitrophenol (4-NP) than electrodes made from graphite. The linear ranges for 4-CP and 4-NP detection were 0.1 to 20.0 μM and 0.5 to 25.0 μM with detection limits of 0.062 μM and 0.11 μM , respectively. Though the sensitivity and LOD were significantly better than that of other electrodes, the linear range and stability were still lower in comparison to them. The sensor created by the authors was successfully applied to detect 4-CP and 4-NP in wastewater samples with promising results [222]. The exfoliated Ti_3AlC_2 was applied in sensor design, without oxidation, and the results demonstrated improved sensitivity of $16.35 \mu\text{A}\cdot\mu\text{M}^{-1}\cdot\text{cm}^{-2}$ and a lower detection limit of 42 nM/L for 4-NP. With an excellent linear sensing range, MXene sensor electrodes were capable of detecting 4-NP in a broad concentration range from 500 nM to 100 M. The selectivity was also high, as the electrode did not react to phenol and its derivatives, like chlorophenol. The characteristics of the sensor were far superior in comparison to graphene-based sensors. The possible mechanism behind the 4-NP oxidation by $\text{Ti}_3\text{C}_2\text{T}_x$ was also described as:



The sensors have also successfully shown reliability and repeatability in continuous monitoring of 4-NP in tap water samples with low interferences [223]. A new heterostructure made of Nb_2CT_x and a Zn-Co-NC-based nanocage was proposed by Runmin Huang et al. The performance of the $\text{Nb}_2\text{CT}_x/\text{Zn-Co-NC}$ -based sensor in the detection 4-NP was advanced by the large specific surface area and conductivity of MXene and the enhanced catalytic activity of the $\text{Nb}_2\text{CT}_x/\text{Zn-Co-NC}$ -based nanocages. The linear range of the sensor was 1 μM to 500 μM , the LOD was 0.070 μM , and the sensitivity was $4.65 \mu\text{A}\cdot\mu\text{M}^{-1}\cdot\text{cm}^{-2}$. The

repeatability of the sensor was also studied, and it was shown that the relative standard deviation (RSD) was less than 3.48% [224].

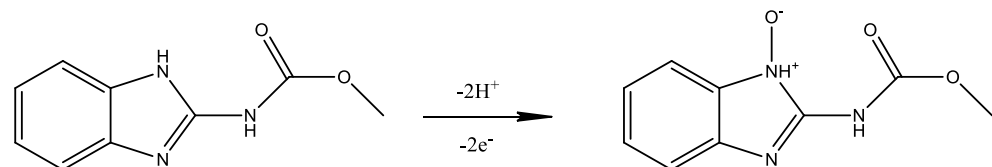
The P. Abdul Rasheed group used a platinum nanoparticle/ $\text{Ti}_3\text{C}_2\text{T}_x$ nanocomposite to measure another phenol derivative—Bisphenol A—and to improve the electrochemical performance and stability of MXene used for the modification of electrodes. The sensor's mechanism involves the oxidation of Bisphenol A [225]:



The proposed sensor had an extremely low LOD (32 nM) in a linear range of 0.05–5 μM , and it was further demonstrated to be successful in detecting Bisphenol A in samples of fresh milk and drinking water [225]. For efficient catechol and hydroquinone detection, Runmin Huang et al. decorated alkalization-intercalated Ti_3C_2 with N-doped porous carbon produced from MOFs. This strategy successfully stopped the Ti_3C_2 sheets from stacking and allowed benzenediol detection, which was based on hydrogen-bond interaction, due to the abundance of C-N and -OH functional groups. The sensor was characterized by a broad linear range of 0.5–150 μM with low detection limits of 4.8 nM ($S/N = 3$) for hydroquinone and 3.1 nM ($S/N = 3$) for catechol. The sensing mechanism revolved around oxidation of hydroquinone and catechol into quinone and 1,2-benzoquinone, respectively. The selectivity of the obtained sensor was high, with an RSD less than 6.6 from a large list of possible interferences (from ions to other phenols like bisphenol A and resorcinol). Compared to sensors from other materials, the obtained one had an adequate linear range and one of the lowest detection limits. Catechol and hydroquinone were also detected by the authors using the acquired sensor in industrial effluent with good recoveries [226].

7.4. Pesticide Sensors

Although pesticide residues pose a serious risk to human health, pesticides play a significant role in agricultural fields; hence, it is necessary to develop sensitive and quick methods for pesticide monitoring. For the purpose of determining the pesticide carbendazim (CBZ), Xiaolong Tu et al. developed a nanoarchitecture of $\text{Ti}_3\text{C}_2\text{T}_x/\text{CNHs}$ (carbon nanohorns)/-CD-MOFs (cyclodextrin-metal-organic frameworks). Due to the synergistic combination of the high electronic conductivity and better catalytic activity from MXene/CNHs and the plentiful electrocatalytic active sites from -CD-MOFs, the MXene/CNHs/-CD-MOFs demonstrated boosted catalytic activity toward CBZ oxidation. The mechanism behind CBZ sensing involved oxidation of the compound on the sensor:



A large linear range from 3.0 nM to 10.0 μM and a low LOD of 1.0 nM ($S/N = 3$) were both determined for the MXene/CNHs/-CD-MOF electrode. The produced sensor was then used in tomato samples, exhibiting high selectivity, repeatability, and long-term stability [227]. Yu Xie et al. used MXene/ERGO composite for CBZ detection to enhance the $\text{Ti}_3\text{C}_2\text{T}_x$ sensing capability. The separated $\text{Ti}_3\text{C}_2\text{T}_x$ layers and particles were tightly connected by the ERGO conductive networks, thus improving the electrochemical reactivity of the electrode. The electrochemical sensor was characterized by a low LOD of 0.67 nM and a large linear range of 2.0 nM to 10.0 μM and was used to measure CBZ in food products [228]. Prussian blue (PB) and $\text{Ti}_3\text{C}_2\text{T}_x$ hybrid composites for H_2O_2 and malathion sensing were created by Ying He et al. In the sensor, $\text{Ti}_3\text{C}_2\text{T}_x$ served as a reducing agent, and the multilayer 2D nanostructure efficiently prevented PB nanoparticles

from aggregating. With a detection limit of 1.3×10^{-16} M, good linearity of malathion was obtained in the range of 1.0×10^{-15} to 1.0×10^{-9} M [229]. Fengnian Zhao et al. created Au-Pd bimetallic nanoparticles through a self-reduction process using ultrathin MXene nanosheets as the reducing agent and support. These nanoparticles advanced the immobilization of acetylcholinesterase and the determination of paraoxon. The MXene/Au-Pd biosensor with an LOD of $1.75 \text{ ng}\cdot\text{L}^{-1}$ showed a good linear relationship with paraoxon concentration from 0.1 to $1000 \text{ }\mu\text{g}\cdot\text{L}^{-1}$, and promising results with cucumber samples were obtained [230]. A new acetylcholinesterase biosensor based on $\text{Ti}_3\text{C}_2\text{T}_x$ nanosheets and chitosan was developed by Liya Zhou et al., and it was found to be suitable for the detection of organophosphate pesticides. The biosensor performed well in terms of malathion detection, with a linearity in the range of 1×10^{-14} – 1×10^{-8} M and an LOD of 0.3×10^{-14} M [231].

8. Optical Sensing

Optical sensing is a promising approach for the detection of chemical compounds because of its high accuracy, strong anti-interference ability, and the non-invasive nature of the measurement [105]. $\text{Ti}_3\text{C}_2\text{T}_x$ -based MXene has a variety of intriguing characteristics that can benefit from optical sensing [232–234]. $\text{Ti}_3\text{C}_2\text{T}_x$ has strong wavelength dependence in its optical absorption zone (from the visible to the short-wave infrared) [235]. In addition, $\text{Ti}_3\text{C}_2\text{T}_x$ has a high intrinsic photothermal conversion efficiency in the infrared irradiation range, allowing the absorbed irradiation power to produce heat effectively [236]. The photoelectric properties of MXenes can also be easily controlled by surface modification [237]. Wide-band optical absorption and good optical modulation are the result of the direct band gap structure of MXene, which may be altered by changing surface functional groups or the number of layers [238,239].

Electrochemiluminescence (ECL) is a sensitive analytical technique that combines the benefits of electrochemistry and luminescence [240–242]. Electrochemically produced intermediates in ECL go through a highly exergonic process to create an excited state, which eventually relaxes to a lower-level state with the emission of light. ECL offers great sensitivity, low cost, and a wide dynamic range; therefore, it can be integrated within simple, easily controllable, and portable analytical instrumentation [243,244]. A prominent biomarker for the diagnosis of chronic myelogenous leukemia is the oncogenic BCR-ABL fusion gene, a distinctive gene of the Ph chromosome [245]. Heterojunction based on $\text{CeO}_2/\text{Ti}_3\text{C}_2\text{T}_x$ was applied to an ECL biosensor for the detection of BCR-ABL. The synthesized heterojunction with strong dispersibility and a large specific surface area synergistically increased the ECL signal of the $\text{S}_2\text{O}_8^{2-}/\text{O}_2$ system and improved the immobilization of biomolecules. The sensor demonstrated a large working concentration range from 1 fM to 100 pM [246].

The process of photoelectrochemistry, or PEC, is defined as the interaction of optical and electrochemical processes wherein an applied light causes electron excitation after charge transfer via photoexcited material [247,248]. The PEC technique uses light as the detecting signal and photocurrent excitation, which is the opposite to ECL [249]. The advantages of sensing based on PEC are the low background signal, easy setup, and excellent sensitivity [250,251]. The PEC-SERS dual-mode biosensor was developed by Fanglei Liu et al. to detect *Staphylococcus aureus* with high accuracy and sensitivity. The method made use of the superior PEC and SERS modes of carbon nitride nanosheet (C_3N_4)/ $\text{Ti}_3\text{C}_2\text{T}_x$ -AuNPs. According to experimental findings, PEC and SERS work well together to amplify *Staphylococcus aureus* detection, with detection ranges of 5 – 10^8 CFU/mL and an LOD of 0.70 CFU/mL for PEC, and 10 – 10^8 CFU/mL and 1.35 CFU/mL for SERS, respectively [252].

The measurement of fluorescence intensity is mostly applied during the action of fluorescence sensors. Typically, these sensors yield low LOD and high sensitivity. Fungal toxins are very dangerous substances due to their mutagenicity, teratogenicity, carcinogenicity, and other characteristics [253,254]. Therefore, the development of efficient methods for

toxin detection is crucial, as the potential contamination of cereals, peanuts, and maize puts human and animal health at risk [255]. A unique fluorescent biosensor for Aflatoxin B1 (AFB1) detection based on the CRISPR/Cas12a system deposited on $\text{Ti}_3\text{C}_2\text{T}_x$ was created by Zhihui Wu et al. When AFB1 was present, the aptamer's preferential binding to it released the activator, which in turn triggered Cas12a's trans-cleavage activity, which indiscriminately cleaved ssDNA on MXenes and restored the fluorescence signal. With a detection range of 0.001 to 80 $\text{ng}\cdot\text{mL}^{-1}$ and a detection limit of 0.92 $\text{pg}\cdot\text{mL}^{-1}$, the fluorescent biosensor was highly versatile [256].

Optical-calorimetry-based techniques are mostly either quantitative or semiquantitative due to their moderate LODs [257], with principal advantages being their inexpensive construction costs and ease of use. Yapeng Li et al. manufactured $\text{Ti}_3\text{C}_2/\text{CuS}$ nanocomposites and used them in a sensor for the detection of cholesterol. When utilized as a peroxidase to catalyze the reaction of 3,3',5,5'-tetramethylbenzidine (TMB) in the presence of H_2O_2 , MXene-based nanocomposites demonstrated peroxidase-like activity and caused a change in color to blue. The cholesterol determination using nanocomposites exhibited a linear range between 10 and 100 μM and LOD of 1.9 μM . Results of the same research illustrated that nanocomposites based on MXene- $\text{Ti}_3\text{C}_2/\text{CuS}$ can be applied in clinical medicine for the detection of H_2O_2 and cholesterol [258].

Surface plasmon resonance (SPR) is a process in which photons of incident light at a specific angle excite the electrons in the metallic surface layer, which then travel parallel to the metal surface [259–261]. The refractive index, or RI, of the substance close to the metal surface determines the specific angle that initiates SPR when there is a constant light source frequency and a thin metal surface. Various analytes can be detected by this technique since a slight alteration in the sensing medium's reflective index will prevent SPR from occurring from a certain angle [262]. Thiol-modified Nb_2C quantum dots ($\text{Nb}_2\text{C-SH QDs}$) have been developed by Rongyuan Chen et al. for use in a novel label-free SPR aptasensor for the detection of SARS-CoV2 N-gene. $\text{Nb}_2\text{C-SH QDs}$ improved the SPR response in addition to having a high bioaffinity for the aptamer. The SPR aptasensor demonstrated a low LOD of 4.9 $\text{pg}\cdot\text{mL}^{-1}$ sensitivity in the concentration range of 0.05 to 100 $\text{ng}\cdot\text{mL}^{-1}$. Additionally, a qualitative examination of N-gene from various sources, such as human serum, seafood, and seawater, was demonstrated using the aptasensor [263].

Raman scattering spectroscopy has distinct advantages over other spectroscopy techniques, including narrow peaks in multicomponent analysis and frequency shifts that offer "fingerprint" information about the chemical structure of an analyte [264]. Nevertheless, the limited sensitivity of Raman spectroscopy renders it useless for the identification of clinical indicators. Surface-enhanced Raman scattering (SERS) occurs when molecules are adsorbed on or near rough metal surfaces or metal-based nanostructures and exhibit an amplification in their Raman signal [262]. To combine the benefits of MXene and metal nanoparticles for SERS, Rongyang Liu et al. created a hybrid biosensor, $\text{Ti}_3\text{C}_2\text{T}_x\text{-AgNPs}$. Dopamine and adenine monitoring demonstrated the SERS sensor's capacity to identify biological molecules; the LOD for adenine was 10^{-8} M, while the LOD for dopamine was 5×10^{-8} M. The biosensor's capacity for detection in serum samples was further demonstrated [265].

9. Conclusions and Outlook

MXenes offer a myriad of advantages that have led to the development of various sensors, including strain, pressure, gas, electrochemical, optical, humidity, and multifunctional sensors. However, there are challenges and issues that need to be addressed for the optimal utilization of MXenes in sensor design. Some of the notable issues include specificity and selectivity, integration within other materials, stability and durability, cost-effectiveness, advanced manufacturing techniques, and difficulties in standardization. One of the challenging issues that needs to be resolved before effectively utilizing MXenes in sensor design is enhancing the specificity and selectivity of MXene-based sensors for certain target analytes. Additionally, achieving high sensitivity without compromising on the ability to

discriminate between different substances is crucial for the reliability of the sensors. While MXenes exhibit excellent properties, combining them with other materials enables the achievement of the desired sensor characteristics. However, ensuring compatibility and efficient integration with other components is still a key consideration for practical sensor designs. The long-term stability and durability of MXene-based sensors, especially under harsh environmental conditions or repeated usage, need further improvement. Ensuring that the sensors maintain their performance over extended periods is essential for practical applications. The production cost of MXenes can be a limiting factor in large-scale applications. Research efforts are ongoing to develop cost-effective methods for MXene synthesis and processing to make them more accessible for widespread sensor deployment; however, at the current time, MXenes remain very expensive materials. Current manufacturing methods for MXene-based sensors involve complex processes. Therefore, streamlining and optimizing these techniques are essential for mass production and commercialization of MXene-based sensors. Further establishing standardized protocols for MXene-based sensor fabrication and testing is crucial for ensuring consistency and comparability across different research studies and applications. The environmental impact of MXene production and disposal is still under consideration. Therefore, a high number of sustainable and eco-friendly approaches for MXene synthesis and integration into sensors are being explored. It is still currently difficult to synthesize MXene-based sensing materials in a controlled manner. For instance, producing MXene nanosheets with specific parameters or surface terminations (currently, a lot of methods result in an abundance of -F groups, which can be damaging to human health and the environment) is still challenging. To this day, the most popular pathways to synthesize MXenes require using or producing hazardous chemicals. Secondly, the chemical stability of MXenes (especially in aqueous solutions) also needs further research and improvements, as the oxidation of MXenes (especially, $Ti_3C_2T_x$) hinders the progress in many applications (for example, biosensors). Finally, more different materials that belong to the MXene family could be applied in sensor design as V-, Mo-, Zr-, Nb-based MXenes and many others can provide a lot of benefits for certain types of sensors, compared to the most commonly used $Ti_3C_2T_x$ -based MXene. Addressing these challenges will contribute to the continued advancement and widespread adoption of MXene-based sensors in various industries. Ongoing research and collaborative efforts are key to overcoming these issues and unlocking the full potential of MXenes in sensor design. Therefore, it is expected that a great number of MXene-based sensors, such as strain, pressure, gas, electrochemical, optical, humidity, and even multifunctional sensors, will be developed by taking advantage of their features, which includes their great electrical conductivity, tunable surface functional groups, a great surface area, superior electrochemical and electrocatalytic capabilities, and remarkable optical properties.

Author Contributions: Conceptualization, I.N., A.R. (Arunas Ramanavicius) and M.P.; methodology, I.N. and S.R.; software, I.N.; validation, I.N., A.R. (Agne Ramanaviciute) and A.R. (Arunas Ramanavicius); formal analysis, I.N. and A.R. (Agne Ramanaviciute); investigation, I.N.; resources, A.R. (Arunas Ramanavicius) and M.P.; data curation, A.R. (Arunas Ramanavicius) and S.R.; writing—original draft preparation, I.N.; writing—review and editing, I.N., A.R. (Agne Ramanaviciute) and A.R. (Arunas Ramanavicius); visualization, I.N.; supervision, A.R. (Agne Ramanaviciute) and S.R.; project administration, A.R. (Arunas Ramanavicius) and S.R.; funding acquisition, A.R. (Agne Ramanaviciute) and S.R. All authors have read and agreed to the published version of the manuscript.

Funding: This project received funding from the Research Council of Lithuania (LMTLT), agreement No S-PD-22-155. A.R. (Arunas Ramanavicius), M.P. and (Agne Ramanaviciute) are thankful to the Horizon Europe MSCA-2021-SE-01 projects (ARGO #101086441 and ESCULAPE #101131147).

Data Availability Statement: No new data were created or analyzed in this study. Data sharing is not applicable to this article.

Conflicts of Interest: The authors declare no conflicts of interest.

Abbreviations

VOC	volatile organic compound
LOD	limit of detection
CNT	carbon nanotube
NW	nanowire
PPy	polypyrrole
HEC	hydroxyethyl cellulose
MWCNTs	multi-walled carbon nanotubes
TPU	thermoplastic polyurethane
PDMS	polydimethylsiloxane
PANI	polyaniline
PANIF	polyaniline fiber
P(VDF-TrFE)	poly(vinylidene fluoride-co-trifluoroethylene)
PVA	polyvinyl alcohol
CMC	sodium carboxymethylcellulose
TA	tannic acid
PVA-CA	catechol-functionalized poly(vinyl alcohol)
PAA	polyacrylic acid
PEDOT	poly(3,4-ethylenedioxythiophene)
PSS	poly(styrene-sulfonate)
ANFs	aramid nanofibers
ZIF-67	zeolitic imidazolate framework-67
PAN	polyacrylonitrile
PE	polyethylene
CTAB	hexadecyl trimethyl ammonium bromide
CMF	carbon sponge
PPNs	polypyrrole nanospheres
TPUEM	thermoplastic polyurethane electrospinning membrane
GO	graphene oxide
rGO	reduced graphene oxide
PS	polystyrene
BC	bacterial cellulose
CA	κ -carrageenan
PAM	polyacrylamide
PHOS	photothermal optical sensor
MZI	Mach-Zehnder interferometer
MKR	micro-fiber knot resonator
RH	relative humidity
TOCNFs	(TEMPO)-oxidized cellulose nanofibers
SAW	surface acoustic wave
MEMS	micro-electromechanical systems
NPs	nanoparticles
ERGO	electrochemically reduced graphene oxide
PDDA	poly(dimethyl diallyl ammonium chloride)
GCE	glassy carbon electrode
CQDs	carbon quantum dots
FL-Cr ₂ CT _x	few-layered two-dimensional chromium carbide
ZIF-8	zeolitic imidazolate framework-8
CC	carbon cloth
4-CP	4-chlorophenol
4-NP	4-nitrophenol
NC	nanocage
RSD	relative standard deviation
MOF	metal-organic framework
CBZ	carbendazim
CNHs	carbon nanohorns
CD-MOFs	cyclodextrin-metal-organic frameworks
PB	Prussian blue

ECL	electrochemiluminescence
PEC	photoelectrochemistry
CFU	Colony-forming unit
CRISPR	clustered regularly interspaced short palindromic repeats
TMB	3,3',5,5'-tetramethylbenzidine
SPR	surface plasmon resonance
SERS	surface-enhanced Raman scattering

References

- Naguib, M.; Kurtoglu, M.; Presser, V.; Lu, J.; Niu, J.; Heon, M.; Hultman, L.; Gogotsi, Y.; Barsoum, M.W. Two-Dimensional Nanocrystals Produced by Exfoliation of Ti_3AlC_2 . *Adv. Mater.* **2011**, *23*, 4248–4253. [[CrossRef](#)] [[PubMed](#)]
- Sun, N.; Zhu, Q.; Anasori, B.; Zhang, P.; Liu, H.; Gogotsi, Y.; Xu, B. MXene-Bonded Flexible Hard Carbon Film as Anode for Stable Na/K-Ion Storage. *Adv. Funct. Mater.* **2019**, *29*, 1906282. [[CrossRef](#)]
- Du, Y.-T.; Kan, X.; Yang, F.; Gan, L.-Y.; Schwingenschlöggl, U. MXene/Graphene Heterostructures as High-Performance Electrodes for Li-Ion Batteries. *ACS Appl. Mater. Interfaces* **2018**, *10*, 32867–32873. [[CrossRef](#)]
- Zhou, Q.; Qian, K.; Fang, J.; Miao, M.; Cao, S.; Feng, X. UV-Light Modulated $\text{Ti}_3\text{C}_2\text{T}_x$ MXene/g- C_3N_4 Heterojunction Film for Electromagnetic Interference Shielding. *Compos. Part. A Appl. Sci. Manuf.* **2020**, *134*, 105899. [[CrossRef](#)]
- Hantanasirisakul, K.; Gogotsi, Y. Electronic and Optical Properties of 2D Transition Metal Carbides and Nitrides (MXenes). *Adv. Mater.* **2018**, *30*, 1804779. [[CrossRef](#)]
- Wen, Y.; Yang, J.; Zou, H.; Fan, Y.; Li, J.; Kuang, Y.; Liu, W.; Zhang, K.; Xiong, L. 2D TiVCT_x Layered Nanosheets Grown on Nickel Foam as Highly Efficient Electrocatalysts for the Hydrogen Evolution Reaction. *RSC Adv.* **2022**, *12*, 23584–23594. [[CrossRef](#)]
- Peng, J.; Chen, X.; Ong, W.-J.; Zhao, X.; Li, N. Surface and Heterointerface Engineering of 2D MXenes and Their Nanocomposites: Insights into Electro- and Photocatalysis. *Chem* **2019**, *5*, 18–50. [[CrossRef](#)]
- Lipatov, A.; Alhabeab, M.; Lu, H.; Zhao, S.; Loes, M.J.; Vorobeva, N.S.; Dall’Agnese, Y.; Gao, Y.; Gruverman, A.; Gogotsi, Y.; et al. Electrical and Elastic Properties of Individual Single-Layer $\text{Nb}_4\text{C}_3\text{T}_x$ MXene Flakes. *Adv. Electron. Mater.* **2020**, *6*, 1901382. [[CrossRef](#)]
- Abdolhosseinzadeh, S.; Jiang, X.; Zhang, H.; Qiu, J.; Zhang, C. Perspectives on Solution Processing of Two-Dimensional MXenes. *Mater. Today* **2021**, *48*, 214–240. [[CrossRef](#)]
- Kamysbayev, V.; Filatov, A.S.; Hu, H.; Rui, X.; Lagunas, F.; Wang, D.; Klie, R.F.; Talapin, D.V. Covalent Surface Modifications and Superconductivity of Two-Dimensional Metal Carbide MXenes. *Science* **2020**, *369*, 979–983. [[CrossRef](#)]
- Shayesteh Zeraati, A.; Mirkhani, S.A.; Sun, P.; Naguib, M.; Braun, P.V.; Sundararaj, U. Improved Synthesis of $\text{Ti}_3\text{C}_2\text{T}_x$ MXenes Resulting in Exceptional Electrical Conductivity, High Synthesis Yield, and Enhanced Capacitance. *Nanoscale* **2021**, *13*, 3572–3580. [[CrossRef](#)]
- Saravanan, P.; Rajeswari, S.; Kumar, J.A.; Rajasimman, M.; Rajamohan, N. Bibliometric Analysis and Recent Trends on MXene Research—A Comprehensive Review. *Chemosphere* **2022**, *286*, 131873. [[CrossRef](#)]
- Naguib, M.; Come, J.; Dyatkin, B.; Presser, V.; Taberna, P.-L.; Simon, P.; Barsoum, M.W.; Gogotsi, Y. MXene: A Promising Transition Metal Carbide Anode for Lithium-Ion Batteries. *Electrochem. Commun.* **2012**, *16*, 61–64. [[CrossRef](#)]
- Lim, K.R.G.; Shekhirev, M.; Wyatt, B.C.; Anasori, B.; Gogotsi, Y.; Seh, Z.W. Fundamentals of MXene Synthesis. *Nat. Synth.* **2022**, *1*, 601–614. [[CrossRef](#)]
- Wei, Y.; Zhang, P.; Soomro, R.A.; Zhu, Q.; Xu, B. Advances in the Synthesis of 2D MXenes. *Adv. Mater.* **2021**, *33*, 2103148. [[CrossRef](#)] [[PubMed](#)]
- Yang, Z.; Liu, A.; Wang, C.; Liu, F.; He, J.; Li, S.; Wang, J.; You, R.; Yan, X.; Sun, P.; et al. Improvement of Gas and Humidity Sensing Properties of Organ-like MXene by Alkaline Treatment. *ACS Sens.* **2019**, *4*, 1261–1269. [[CrossRef](#)] [[PubMed](#)]
- Caffrey, N.M. Effect of Mixed Surface Terminations on the Structural and Electrochemical Properties of Two-Dimensional $\text{Ti}_3\text{C}_2\text{T}_2$ and V_2CT_2 MXenes Multilayers. *Nanoscale* **2018**, *10*, 13520–13530. [[CrossRef](#)]
- Seh, Z.W.; Fredrickson, K.D.; Anasori, B.; Kibsgaard, J.; Strickler, A.L.; Lukatskaya, M.R.; Gogotsi, Y.; Jaramillo, T.F.; Vojvodic, A. Two-Dimensional Molybdenum Carbide (MXene) as an Efficient Electrocatalyst for Hydrogen Evolution. *ACS Energy Lett.* **2016**, *1*, 589–594. [[CrossRef](#)]
- Rasheed, P.A.; Pandey, R.P.; Banat, F.; Hasan, S.W. Recent Advances in Niobium MXenes: Synthesis, Properties, and Emerging Applications. *Matter* **2022**, *5*, 546–572. [[CrossRef](#)]
- Jiang, L.; Zhou, D.; Yang, J.; Zhou, S.; Wang, H.; Yuan, X.; Liang, J.; Li, X.; Chen, Y.; Li, H. 2D Single- and Few-Layered MXenes: Synthesis, Applications and Perspectives. *J. Mater. Chem. A Mater.* **2022**, *10*, 13651–13672. [[CrossRef](#)]
- Pogorielov, M.; Smyrnova, K.; Kyrylenko, S.; Gogotsi, O.; Zahorodna, V.; Pogrebnjak, A. MXenes—A New Class of Two-Dimensional Materials: Structure, Properties and Potential Applications. *Nanomaterials* **2021**, *11*, 3412. [[CrossRef](#)]
- Ghidiu, M.; Naguib, M.; Shi, C.; Mashtalir, O.; Pan, L.M.; Zhang, B.; Yang, J.; Gogotsi, Y.; Billinge, S.J.L.; Barsoum, M.W. Synthesis and Characterization of Two-Dimensional Nb_4C_3 (MXene). *Chem. Commun.* **2014**, *50*, 9517–9520. [[CrossRef](#)]
- Lukatskaya, M.R.; Mashtalir, O.; Ren, C.E.; Dall’Agnese, Y.; Rozier, P.; Taberna, P.L.; Naguib, M.; Simon, P.; Barsoum, M.W.; Gogotsi, Y. Cation Intercalation and High Volumetric Capacitance of Two-Dimensional Titanium Carbide. *Science* **2013**, *341*, 1502–1505. [[CrossRef](#)]

24. Mashtalir, O.; Naguib, M.; Dyatkin, B.; Gogotsi, Y.; Barsoum, M.W. Kinetics of Aluminum Extraction from Ti_3AlC_2 in Hydrofluoric Acid. *Mater. Chem. Phys.* **2013**, *139*, 147–152. [[CrossRef](#)]
25. Halim, J.; Kota, S.; Lukatskaya, M.R.; Naguib, M.; Zhao, M.-Q.; Moon, E.J.; Pitock, J.; Nanda, J.; May, S.J.; Gogotsi, Y.; et al. Synthesis and Characterization of 2D Molybdenum Carbide (MXene). *Adv. Funct. Mater.* **2016**, *26*, 3118–3127. [[CrossRef](#)]
26. Li, T.; Yao, L.; Liu, Q.; Gu, J.; Luo, R.; Li, J.; Yan, X.; Wang, W.; Liu, P.; Chen, B.; et al. Fluorine-Free Synthesis of High-Purity Ti_3C_2Tx (T=OH, O) via Alkali Treatment. *Angew. Chem. Int. Ed.* **2018**, *57*, 6115–6119. [[CrossRef](#)] [[PubMed](#)]
27. Li, G.; Tan, L.; Zhang, Y.; Wu, B.; Li, L. Highly Efficiently Delaminated Single-Layered MXene Nanosheets with Large Lateral Size. *Langmuir* **2017**, *33*, 9000–9006. [[CrossRef](#)] [[PubMed](#)]
28. Li, Y.; Shao, H.; Lin, Z.; Lu, J.; Liu, L.; Duployer, B.; Persson, P.O.Å.; Eklund, P.; Hultman, L.; Li, M.; et al. A General Lewis Acidic Etching Route for Preparing MXenes with Enhanced Electrochemical Performance in Non-Aqueous Electrolyte. *Nat. Mater.* **2020**, *19*, 894–899. [[CrossRef](#)] [[PubMed](#)]
29. Li, M.; Lu, J.; Luo, K.; Li, Y.; Chang, K.; Chen, K.; Zhou, J.; Rosen, J.; Hultman, L.; Eklund, P.; et al. Element Replacement Approach by Reaction with Lewis Acidic Molten Salts to Synthesize Nanolaminated MAX Phases and MXenes. *J. Am. Chem. Soc.* **2019**, *141*, 4730–4737. [[CrossRef](#)] [[PubMed](#)]
30. Pang, S.-Y.; Wong, Y.-T.; Yuan, S.; Liu, Y.; Tsang, M.-K.; Yang, Z.; Huang, H.; Wong, W.-T.; Hao, J. Universal Strategy for HF-Free Facile and Rapid Synthesis of Two-Dimensional MXenes as Multifunctional Energy Materials. *J. Am. Chem. Soc.* **2019**, *141*, 9610–9616. [[CrossRef](#)] [[PubMed](#)]
31. Yang, S.; Zhang, P.; Wang, F.; Ricciardulli, A.G.; Lohe, M.R.; Blom, P.W.M.; Feng, X. Fluoride-Free Synthesis of Two-Dimensional Titanium Carbide (MXene) Using a Binary Aqueous System. *Angew. Chem. Int. Ed.* **2018**, *57*, 15491–15495. [[CrossRef](#)]
32. Shi, H.; Zhang, P.; Liu, Z.; Park, S.; Lohe, M.R.; Wu, Y.; Shaygan Nia, A.; Yang, S.; Feng, X. Ambient-Stable Two-Dimensional Titanium Carbide (MXene) Enabled by Iodine Etching. *Angew. Chem. Int. Ed.* **2021**, *60*, 8689–8693. [[CrossRef](#)] [[PubMed](#)]
33. Mei, J.; Ayoko, G.A.; Hu, C.; Bell, J.M.; Sun, Z. Two-Dimensional Fluorine-Free Mesoporous Mo_2C MXene via UV-Induced Selective Etching of Mo_2Ga_2C for Energy Storage. *Sustain. Mater. Technol.* **2020**, *25*, e00156. [[CrossRef](#)]
34. Marian, M.; Song, G.C.; Wang, B.; Fuenzalida, V.M.; Krauß, S.; Merle, B.; Tremmel, S.; Wartzack, S.; Yu, J.; Rosenkranz, A. Effective Usage of 2D MXene Nanosheets as Solid Lubricant—Influence of Contact Pressure and Relative Humidity. *Appl. Surf. Sci.* **2020**, *531*, 147311. [[CrossRef](#)]
35. Wang, B.; Zhou, A.; Liu, F.; Cao, J.; Wang, L.; Hu, Q. Carbon Dioxide Adsorption of Two-Dimensional Carbide MXenes. *J. Adv. Ceram.* **2018**, *7*, 237–245. [[CrossRef](#)]
36. Naguib, M.; Unocic, R.R.; Armstrong, B.L.; Nanda, J. Large-Scale Delamination of Multi-Layers Transition Metal Carbides and Carbonitrides “MXenes.” *Dalton Trans.* **2015**, *44*, 9353–9358. [[CrossRef](#)] [[PubMed](#)]
37. Mashtalir, O.; Lukatskaya, M.R.; Zhao, M.-Q.; Barsoum, M.W.; Gogotsi, Y. Amine-Assisted Delamination of Nb_2C MXene for Li-Ion Energy Storage Devices. *Adv. Mater.* **2015**, *27*, 3501–3506. [[CrossRef](#)]
38. Wang, H.; Zhang, J.; Wu, Y.; Huang, H.; Li, G.; Zhang, X.; Wang, Z. Surface Modified MXene Ti_3C_2 Multilayers by Aryl Diazonium Salts Leading to Large-Scale Delamination. *Appl. Surf. Sci.* **2016**, *384*, 287–293. [[CrossRef](#)]
39. Pazniak, H.; Plugin, I.A.; Sheverdyeva, P.M.; Rapenne, L.; Varezchnikov, A.S.; Agresti, A.; Pescetelli, S.; Moras, P.; Kostin, K.B.; Gorokhovskiy, A.V.; et al. Alcohol Vapor Sensor Based on Quasi-2D Nb_2O_5 Derived from Oxidized Nb_2CT_x MXenes. *Sensors* **2024**, *24*, 38. [[CrossRef](#)]
40. Jolly, S.; Paranthaman, M.P.; Naguib, M. Synthesis of $Ti_3C_2T_z$ MXene from Low-Cost and Environmentally Friendly Precursors. *Mater. Today Adv.* **2021**, *10*, 100139. [[CrossRef](#)]
41. Li, C.; Kota, S.; Hu, C.; Barsoum, M. On the Synthesis of Low-Cost, Titanium-Based MXenes. *J. Ceram. Sci. Technol.* **2016**, *7*, 7–10. [[CrossRef](#)]
42. Ramanavicius, S.; Ramanavicius, A. Progress and Insights in the Application of MXenes as New 2D Nano-Materials Suitable for Biosensors and Biofuel Cell Design. *Int. J. Mol. Sci.* **2020**, *21*, 9224. [[CrossRef](#)]
43. Guo, B.; He, S.; Yao, M.; Tan, Z.; Li, X.; Liu, M.; Yu, C.; Liang, L.; Zhao, Z.; Guo, Z.; et al. MXene-Containing Anisotropic Hydrogels Strain Sensors with Enhanced Sensing Performance for Human Motion Monitoring and Wireless Transmission. *Chem. Eng. J.* **2023**, *461*, 142099. [[CrossRef](#)]
44. Yi, J.; Xianyu, Y. Gold Nanomaterials-Implemented Wearable Sensors for Healthcare Applications. *Adv. Funct. Mater.* **2022**, *32*, 2113012. [[CrossRef](#)]
45. Wu, L.; Wang, L.; Guo, Z.; Luo, J.; Xue, H.; Gao, J. Durable and Multifunctional Superhydrophobic Coatings with Excellent Joule Heating and Electromagnetic Interference Shielding Performance for Flexible Sensing Electronics. *ACS Appl. Mater. Interfaces* **2019**, *11*, 34338–34347. [[CrossRef](#)] [[PubMed](#)]
46. Tang, J.; Wu, Y.; Ma, S.; Yan, T.; Pan, Z. Flexible Strain Sensor Based on CNT/TPU Composite Nanofiber Yarn for Smart Sports Bandage. *Compos. B Eng.* **2022**, *232*, 109605. [[CrossRef](#)]
47. Duan, Q.; Lan, B.; Lv, Y. Highly Dispersed, Adhesive Carbon Nanotube Ink for Strain and Pressure Sensors. *ACS Appl. Mater. Interfaces* **2022**, *14*, 1973–1982. [[CrossRef](#)]
48. Zheng, X.; Cao, W.; Hong, X.; Zou, L.; Liu, Z.; Wang, P.; Li, C. Versatile Electronic Textile Enabled by a Mixed-Dimensional Assembly Strategy. *Small* **2023**, *19*, 2208134. [[CrossRef](#)]

49. Li, X.; Zhao, B.; Qin, W.; Yang, M.; Feng, L.; Gu, C.; Tian, Z.; Liu, H.; Guo, X.; Zhang, Y.; et al. MXene $\text{Ti}_3\text{C}_2\text{T}_x$, EGIIn, and Carbon Nanotube Composites on Polyurethane Substrates for Strain Sensing, Electromagnetic Interference Shielding, and Joule Heating. *ACS Appl. Nano Mater.* **2023**, *6*, 14459–14468. [[CrossRef](#)]
50. Pu, J.-H.; Zhao, X.; Zha, X.-J.; Bai, L.; Ke, K.; Bao, R.-Y.; Liu, Z.-Y.; Yang, M.-B.; Yang, W. Multilayer Structured AgNW/WPU-MXene Fiber Strain Sensors with Ultrahigh Sensitivity and a Wide Operating Range for Wearable Monitoring and Healthcare. *J. Mater. Chem. A Mater.* **2019**, *7*, 15913–15923. [[CrossRef](#)]
51. Yang, Y.; Cao, Z.; He, P.; Shi, L.; Ding, G.; Wang, R.; Sun, J. $\text{Ti}_3\text{C}_2\text{T}_x$ MXene-Graphene Composite Films for Wearable Strain Sensors Featured with High Sensitivity and Large Range of Linear Response. *Nano Energy* **2019**, *66*, 104134. [[CrossRef](#)]
52. Cai, Y.; Shen, J.; Ge, G.; Zhang, Y.; Jin, W.; Huang, W.; Shao, J.; Yang, J.; Dong, X. Stretchable $\text{Ti}_3\text{C}_2\text{T}_x$ MXene/Carbon Nanotube Composite Based Strain Sensor with Ultrahigh Sensitivity and Tunable Sensing Range. *ACS Nano* **2018**, *12*, 56–62. [[CrossRef](#)]
53. Xu, X.; Chen, Y.; He, P.; Wang, S.; Ling, K.; Liu, L.; Lei, P.; Huang, X.; Zhao, H.; Cao, J.; et al. Wearable CNT/ $\text{Ti}_3\text{C}_2\text{T}_x$ MXene/PDMS Composite Strain Sensor with Enhanced Stability for Real-Time Human Healthcare Monitoring. *Nano Res.* **2021**, *14*, 2875–2883. [[CrossRef](#)]
54. Cao, J.; Jiang, Y.; Li, X.; Yuan, X.; Zhang, J.; He, Q.; Ye, F.; Luo, G.; Guo, S.; Zhang, Y.; et al. A Flexible and Stretchable MXene/Waterborne Polyurethane Composite-Coated Fiber Strain Sensor for Wearable Motion and Healthcare Monitoring. *Sensors* **2024**, *24*, 271. [[CrossRef](#)]
55. Yang, H.; Xiao, X.; Li, Z.; Li, K.; Cheng, N.; Li, S.; Low, J.H.; Jing, L.; Fu, X.; Achavananthadith, S.; et al. Wireless $\text{Ti}_3\text{C}_2\text{T}_x$ MXene Strain Sensor with Ultrahigh Sensitivity and Designated Working Windows for Soft Exoskeletons. *ACS Nano* **2020**, *14*, 11860–11875. [[CrossRef](#)]
56. Liao, H.; Guo, X.; Wan, P.; Yu, G. Conductive MXene Nanocomposite Organohydrogel for Flexible, Healable, Low-Temperature Tolerant Strain Sensors. *Adv. Funct. Mater.* **2019**, *29*, 1904507. [[CrossRef](#)]
57. Yang, C.; Zhang, D.; Wang, D.; Luan, H.; Chen, X.; Yan, W. In Situ Polymerized MXene/Polypyrrole/Hydroxyethyl Cellulose-Based Flexible Strain Sensor Enabled by Machine Learning for Handwriting Recognition. *ACS Appl. Mater. Interfaces* **2023**, *15*, 5811–5821. [[CrossRef](#)] [[PubMed](#)]
58. Wang, H.; Zhou, R.; Li, D.; Zhang, L.; Ren, G.; Wang, L.; Liu, J.; Wang, D.; Tang, Z.; Lu, G.; et al. High-Performance Foam-Shaped Strain Sensor Based on Carbon Nanotubes and $\text{Ti}_3\text{C}_2\text{T}_x$ MXene for the Monitoring of Human Activities. *ACS Nano* **2021**, *15*, 9690–9700. [[CrossRef](#)] [[PubMed](#)]
59. Yang, K.; Yin, F.; Xia, D.; Peng, H.; Yang, J.; Yuan, W. A Highly Flexible and Multifunctional Strain Sensor Based on a Network-Structured MXene/Polyurethane Mat with Ultra-High Sensitivity and a Broad Sensing Range. *Nanoscale* **2019**, *11*, 9949–9957. [[CrossRef](#)] [[PubMed](#)]
60. Chao, M.; Wang, Y.; Ma, D.; Wu, X.; Zhang, W.; Zhang, L.; Wan, P. Wearable MXene Nanocomposites-Based Strain Sensor with Tile-like Stacked Hierarchical Microstructure for Broad-Range Ultrasensitive Sensing. *Nano Energy* **2020**, *78*, 105187. [[CrossRef](#)]
61. Bu, Y.; Shen, T.; Yang, W.; Yang, S.; Zhao, Y.; Liu, H.; Zheng, Y.; Liu, C.; Shen, C. Ultrasensitive Strain Sensor Based on Superhydrophobic Microcracked Conductive $\text{Ti}_3\text{C}_2\text{T}_x$ MXene/Paper for Human-Motion Monitoring and E-Skin. *Sci. Bull.* **2021**, *66*, 1849–1857. [[CrossRef](#)] [[PubMed](#)]
62. Fu, X.; Li, L.; Chen, S.; Xu, H.; Li, J.; Shulga, V.; Han, W. Knitted $\text{Ti}_3\text{C}_2\text{T}_x$ MXene Based Fiber Strain Sensor for Human-Computer Interaction. *J. Colloid. Interface Sci.* **2021**, *604*, 643–649. [[CrossRef](#)] [[PubMed](#)]
63. Kong, D.; El-Bahy, Z.M.; Algadi, H.; Li, T.; El-Bahy, S.M.; Nassan, M.A.; Li, J.; Faheim, A.A.; Li, A.; Xu, C.; et al. Highly Sensitive Strain Sensors with Wide Operation Range from Strong MXene-Composited Polyvinyl Alcohol/Sodium Carboxymethylcellulose Double Network Hydrogel. *Adv. Compos. Hybrid. Mater.* **2022**, *5*, 1976–1987. [[CrossRef](#)]
64. Chae, A.; Murali, G.; Lee, S.-Y.; Gwak, J.; Kim, S.J.; Jeong, Y.J.; Kang, H.; Park, S.; Lee, A.S.; Koh, D.-Y.; et al. Highly Oxidation-Resistant and Self-Healable MXene-Based Hydrogels for Wearable Strain Sensor. *Adv. Funct. Mater.* **2023**, *33*, 2213382. [[CrossRef](#)]
65. Peng, W.; Pan, X.; Liu, X.; Gao, Y.; Lu, T.; Li, J.; Xu, M.; Pan, L. A Moisture Self-Regenerative, Ultra-Low Temperature Anti-Freezing and Self-Adhesive Polyvinyl Alcohol/Polyacrylamide/ CaCl_2 /MXene Ionotronics Hydrogel for Bionic Skin Strain Sensor. *J. Colloid. Interface Sci.* **2023**, *634*, 782–792. [[CrossRef](#)] [[PubMed](#)]
66. Dong, L.; Zhou, X.; Zheng, S.; Luo, Z.; Nie, Y.; Feng, X.; Zhu, J.; Wang, Z.; Lu, X.; Mu, L. Liquid Metal @ Mxene Spring Supports Ionic Gel with Excellent Mechanical Properties for High-Sensitivity Wearable Strain Sensor. *Chem. Eng. J.* **2023**, *458*, 141370. [[CrossRef](#)]
67. Liang, J.; He, J.; Xin, Y.; Gao, W.; Zeng, G.; He, X. MXene Reinforced PAA/PEDOT:PSS/MXene Conductive Hydrogel for Highly Sensitive Strain Sensors. *Macromol. Mater. Eng.* **2023**, *308*, 2200519. [[CrossRef](#)]
68. Qin, W.; Geng, J.; Lin, C.; Li, G.; Peng, H.; Xue, Y.; Zhou, B.; Liu, G. Flexible Multifunctional TPU Strain Sensors with Improved Sensitivity and Wide Sensing Range Based on MXene/AgNWs. *J. Mater. Sci. Mater. Electron.* **2023**, *34*, 564. [[CrossRef](#)]
69. Seesaard, T.; Wongchoosuk, C. Flexible and Stretchable Pressure Sensors: From Basic Principles to State-of-the-Art Applications. *Micromachines* **2023**, *14*, 1638. [[CrossRef](#)]
70. Ma, Z.; Zhang, Y.; Zhang, K.; Deng, H.; Fu, Q. Recent Progress in Flexible Capacitive Sensors: Structures and Properties. *Nano Mater. Sci.* **2023**, *5*, 265–277. [[CrossRef](#)]
71. Wu, Y.; Ma, Y.; Zheng, H.; Ramakrishna, S. Piezoelectric Materials for Flexible and Wearable Electronics: A Review. *Mater. Des.* **2021**, *211*, 110164. [[CrossRef](#)]

72. Garcia, C.; Trendafilova, I.; Guzman de Villoria, R.; Sanchez del Rio, J. Self-Powered Pressure Sensor Based on the Triboelectric Effect and Its Analysis Using Dynamic Mechanical Analysis. *Nano Energy* **2018**, *50*, 401–409. [[CrossRef](#)]
73. Trung, T.Q.; Lee, N.-E. Flexible and Stretchable Physical Sensor Integrated Platforms for Wearable Human-Activity Monitoring and Personal Healthcare. *Adv. Mater.* **2016**, *28*, 4338–4372. [[CrossRef](#)] [[PubMed](#)]
74. Liang, G.; Ruan, Z.; Liu, Z.; Li, H.; Wang, Z.; Tang, Z.; Mo, F.; Yang, Q.; Ma, L.; Wang, D.; et al. Toward Multifunctional and Wearable Smart Skins with Energy-Harvesting, Touch-Sensing, and Exteroception-Visualizing Capabilities by an All-Polymer Design. *Adv. Electron. Mater.* **2019**, *5*, 1900553. [[CrossRef](#)]
75. Fiorillo, A.S.; Critello, C.D.; Pullano, S.A. Theory, Technology and Applications of Piezoresistive Sensors: A Review. *Sens. Actuators A Phys.* **2018**, *281*, 156–175. [[CrossRef](#)]
76. Li, H.; Wu, K.; Xu, Z.; Wang, Z.; Meng, Y.; Li, L. Ultrahigh-Sensitivity Piezoresistive Pressure Sensors for Detection of Tiny Pressure. *ACS Appl. Mater. Interfaces* **2018**, *10*, 20826–20834. [[CrossRef](#)]
77. Zhang, Y.; Wang, L.; Zhao, L.; Wang, K.; Zheng, Y.; Yuan, Z.; Wang, D.; Fu, X.; Shen, G.; Han, W. Flexible Self-Powered Integrated Sensing System with 3D Periodic Ordered Black Phosphorus@MXene Thin-Films. *Adv. Mater.* **2021**, *33*, 2007890. [[CrossRef](#)] [[PubMed](#)]
78. Zhao, Y.; Liu, Y.; Li, Y.; Hao, Q. Development and Application of Resistance Strain Force Sensors. *Sensors* **2020**, *20*, 5826. [[CrossRef](#)]
79. Wu, Z.; Wei, L.; Tang, S.; Xiong, Y.; Qin, X.; Luo, J.; Fang, J.; Wang, X. Recent Progress in $Ti_3C_2T_x$ MXene-Based Flexible Pressure Sensors. *ACS Nano* **2021**, *15*, 18880–18894. [[CrossRef](#)]
80. Zou, Y.; Chen, Z.; Guo, X.; Peng, Z.; Yu, C.; Zhong, W. Mechanically Robust and Elastic Graphene/Aramid Nanofiber/Polyaniline Nanotube Aerogels for Pressure Sensors. *ACS Appl. Mater. Interfaces* **2022**, *14*, 17858–17868. [[CrossRef](#)]
81. Fu, X.; Li, J.; Li, D.; Zhao, L.; Yuan, Z.; Shulga, V.; Han, W.; Wang, L. MXene/ZIF-67/PAN Nanofiber Film for Ultra-Sensitive Pressure Sensors. *ACS Appl. Mater. Interfaces* **2022**, *14*, 12367–12374. [[CrossRef](#)] [[PubMed](#)]
82. Lei, D.; Liu, N.; Su, T.; Zhang, Q.; Wang, L.; Ren, Z.; Gao, Y. Roles of MXene in Pressure Sensing: Preparation, Composite Structure Design, and Mechanism. *Adv. Mater.* **2022**, *34*, 2110608. [[CrossRef](#)] [[PubMed](#)]
83. Zheng, Y.; Yin, R.; Zhao, Y.; Liu, H.; Zhang, D.; Shi, X.; Zhang, B.; Liu, C.; Shen, C. Conductive MXene/Cotton Fabric Based Pressure Sensor with Both High Sensitivity and Wide Sensing Range for Human Motion Detection and E-Skin. *Chem. Eng. J.* **2021**, *420*, 127720. [[CrossRef](#)]
84. Xu, Z.; Zhang, D.; Li, Z.; Du, C.; Yang, Y.; Zhang, B.; Zhao, W. Waterproof Flexible Pressure Sensors Based on Electrostatic Self-Assembled MXene/NH₂-CNTs for Motion Monitoring and Electronic Skin. *ACS Appl. Mater. Interfaces* **2023**, *15*, 32569–32579. [[CrossRef](#)] [[PubMed](#)]
85. Wang, L.; Zhang, M.; Yang, B.; Tan, J.; Ding, X. Highly Compressible, Thermally Stable, Light-Weight, and Robust Aramid Nanofibers/ Ti_3AlC_2 MXene Composite Aerogel for Sensitive Pressure Sensor. *ACS Nano* **2020**, *14*, 10633–10647. [[CrossRef](#)]
86. Yin, T.; Cheng, Y.; Hou, Y.; Sun, L.; Ma, Y.; Su, J.; Zhang, Z.; Liu, N.; Li, L.; Gao, Y. 3D Porous Structure in MXene/PANI Foam for a High-Performance Flexible Pressure Sensor. *Small* **2022**, *18*, 2204806. [[CrossRef](#)]
87. Li, G.; Sun, F.; Zhao, S.; Xu, R.; Wang, H.; Qu, L.; Tian, M. Autonomous Electroluminescent Textile for Visual Interaction and Environmental Warning. *Nano Lett.* **2023**, *23*, 8436–8444. [[CrossRef](#)]
88. Guo, D.; Mu, C.; Liu, Q.; Wang, B.; Xiang, J.; Nie, A.; Zhai, K.; Shu, Y.; Xue, T.; Wen, F.; et al. Aramid Nanofiber/Polypyrrole Composite Films for Broadband EMI Shielding, Wearable Electronics, Joule Heating, and Photothermal Conversion. *ACS Appl. Nano Mater.* **2023**, *6*, 15108–15118. [[CrossRef](#)]
89. Ma, Y.; Liu, N.; Li, L.; Hu, X.; Zou, Z.; Wang, J.; Luo, S.; Gao, Y. A Highly Flexible and Sensitive Piezoresistive Sensor Based on MXene with Greatly Changed Interlayer Distances. *Nat. Commun.* **2017**, *8*, 1207. [[CrossRef](#)]
90. Pei, Y.; Wang, K.; Hui, Z.; Pan, H.; Zhou, J.; Sun, G. Blowing up $Ti_3C_2T_x$ MXene Membrane for Robust Sound Detection. *Appl. Phys. Lett.* **2023**, *122*, 083501. [[CrossRef](#)]
91. Gou, G.-Y.; Li, X.-S.; Jian, J.-M.; Tian, H.; Wu, F.; Ren, J.; Geng, X.-S.; Xu, J.-D.; Qiao, Y.-C.; Yan, Z.-Y.; et al. Two-Stage Amplification of an Ultrasensitive MXene-Based Intelligent Artificial Eardrum. *Sci. Adv.* **2024**, *8*, eabn2156. [[CrossRef](#)]
92. Bilibana, M.P. Electrochemical Properties of MXenes and Applications. *Adv. Sens. Energy Mater.* **2023**, *2*, 100080. [[CrossRef](#)]
93. Hajian, S.; Maddipatla, D.; Narakathu, B.B.; Atashbar, M.Z. MXene-Based Flexible Sensors: A Review. *Front. Sens.* **2022**, *3*, 1006749. [[CrossRef](#)]
94. Qi, Z.; Zhang, T.; Zhang, X.-D.; Xu, Q.; Cao, K.; Chen, R. MXene-Based Flexible Pressure Sensor with Piezoresistive Properties Significantly Enhanced by Atomic Layer Infiltration. *Nano Mater. Sci.* **2023**, *5*, 439–446. [[CrossRef](#)]
95. Li, C.; Gu, H.; Ji, Z.; Zhang, L.; Xu, R.; Gao, J.; Jiang, Y. Hierarchically Structured MXene Nanosheets on Carbon Sponges with a Synergistic Effect of Electrostatic Adsorption and Capillary Action for Highly Sensitive Pressure Sensors. *ACS Appl. Nano Mater.* **2023**, *6*, 13482–13491. [[CrossRef](#)]
96. Cheng, H.; Yang, C.; Chu, J.; Zhou, H.; Wang, C. Multifunctional $Ti_3C_2T_x$ MXene/Nanospheres/ $Ti_3C_2T_x$ MXene/Thermoplastic Polyurethane Electrospinning Membrane Inspired by Bean Pod Structure for EMI Shielding and Pressure Sensing. *Sens. Actuators A Phys.* **2023**, *353*, 114226. [[CrossRef](#)]
97. Xie, Y.; Cheng, Y.; Ma, Y.; Wang, J.; Zou, J.; Wu, H.; Yue, Y.; Li, B.; Gao, Y.; Zhang, X.; et al. 3D MXene-Based Flexible Network for High-Performance Pressure Sensor with a Wide Temperature Range. *Adv. Sci.* **2023**, *10*, 2205303. [[CrossRef](#)]
98. Li, L.; Cheng, Y.; Cao, H.; Liang, Z.; Liu, Z.; Yan, S.; Li, L.; Jia, S.; Wang, J.; Gao, Y. MXene/RGO/PS Spheres Multiple Physical Networks as High-Performance Pressure Sensor. *Nano Energy* **2022**, *95*, 106986. [[CrossRef](#)]

99. Yang, J.; Li, H.; Cheng, J.; He, T.; Li, J.; Wang, B. Nanocellulose Intercalation to Boost the Performance of MXene Pressure Sensor for Human Interactive Monitoring. *J. Mater. Sci.* **2021**, *56*, 13859–13873. [[CrossRef](#)]
100. Cao, Z.; Yang, Y.; Zheng, Y.; Wu, W.; Xu, F.; Wang, R.; Sun, J. Highly Flexible and Sensitive Temperature Sensors Based on $\text{Ti}_3\text{C}_2\text{T}_x$ (MXene) for Electronic Skin. *J. Mater. Chem. A Mater.* **2019**, *7*, 25314–25323. [[CrossRef](#)]
101. Zhao, L.; Fu, X.; Xu, H.; Zheng, Y.; Han, W.; Wang, L. Tissue-Like Sodium Alginate-Coated 2D MXene-Based Flexible Temperature Sensors for Full-Range Temperature Monitoring. *Adv. Mater. Technol.* **2022**, *7*, 2101740. [[CrossRef](#)]
102. Wang, Z.; Zou, X.; Yang, Z.; Wang, J.; Chen, Q.; Pei, C.; Wang, Z.; Dong, M.; Zhang, J.; Li, H.; et al. Highly Sensitive Temperature Detection Based on a Frost- and Dehydration-Resistive Ion-Doped Hydrogel-MXene Composite. *ACS Appl. Mater. Interfaces* **2023**, *15*, 35525–35533. [[CrossRef](#)]
103. Liu, H.; Yang, N.; Zhang, Q.; Wang, F.; Yan, X.; Zhang, X.; Cheng, T. A High-Performance Wearable Ag/ $\text{Ti}_3\text{C}_2\text{T}_x$ MXene-Based Fiber Sensor for Temperature Sensing, Pressure Sensing, and Human Motion Detection. *IEEE Trans. Instrum. Meas.* **2022**, *71*, 9512608. [[CrossRef](#)]
104. Saeidi-Javash, M.; Du, Y.; Zeng, M.; Wyatt, B.C.; Zhang, B.; Kempf, N.; Anasori, B.; Zhang, Y. All-Printed MXene–Graphene Nanosheet-Based Bimodal Sensors for Simultaneous Strain and Temperature Sensing. *ACS Appl. Electron. Mater.* **2021**, *3*, 2341–2348. [[CrossRef](#)]
105. Zuo, Y.; Gao, Y.; Qin, S.; Wang, Z.; Zhou, D.; Li, Z.; Yu, Y.; Shao, M.; Zhang, X. Broadband Multi-Wavelength Optical Sensing Based on Photothermal Effect of 2D MXene Films. *Nanophotonics* **2020**, *9*, 123–131. [[CrossRef](#)]
106. Chen, S.; Ran, J.; Zheng, T.; Wu, Q. Ultracompact MXene V2C-Improved Temperature Sensor by a Runway-Type Microfiber Knot Resonator. *Nanomaterials* **2023**, *13*, 2354. [[CrossRef](#)] [[PubMed](#)]
107. Wu, Q.; Ran, J.; Zheng, T.; Wu, H.; Liao, Y.; Wang, F.; Chen, S. MXene V2C-Coated Runway-Type Microfiber Knot Resonator for an All-Optical Temperature Sensor. *RSC Adv.* **2023**, *13*, 19366–19372. [[CrossRef](#)] [[PubMed](#)]
108. Yuan, X.; Zhang, M.; Wu, Y. MXene-Based Sensors for Detecting Human Physiological Information. *Sens. Mater.* **2020**, *32*, 4047–4065. [[CrossRef](#)]
109. Tai, Y.; Lubineau, G. Human-Finger Electronics Based on Opposing Humidity-Resistance Responses in Carbon Nanofilms. *Small* **2017**, *13*, 1603486. [[CrossRef](#)] [[PubMed](#)]
110. Wu, J.; Wu, Z.; Xu, H.; Wu, Q.; Liu, C.; Yang, B.-R.; Gui, X.; Xie, X.; Tao, K.; Shen, Y.; et al. An Intrinsically Stretchable Humidity Sensor Based on Anti-Drying, Self-Healing and Transparent Organohydrogels. *Mater. Horiz.* **2019**, *6*, 595–603. [[CrossRef](#)]
111. Wu, J.; Sun, Y.-M.; Wu, Z.; Li, X.; Wang, N.; Tao, K.; Wang, G.P. Carbon Nanocoil-Based Fast-Response and Flexible Humidity Sensor for Multifunctional Applications. *ACS Appl. Mater. Interfaces* **2019**, *11*, 4242–4251. [[CrossRef](#)] [[PubMed](#)]
112. Li, J.; Yuan, X.; Lin, C.; Yang, Y.; Xu, L.; Du, X.; Xie, J.; Lin, J.; Sun, J. Achieving High Pseudocapacitance of 2D Titanium Carbide (MXene) by Cation Intercalation and Surface Modification. *Adv. Energy Mater.* **2017**, *7*, 1602725. [[CrossRef](#)]
113. Célérier, S.; Hurand, S.; Garnero, C.; Morisset, S.; Benchakar, M.; Habrioux, A.; Chartier, P.; Mauchamp, V.; Findling, N.; Lanson, B.; et al. Hydration of $\text{Ti}_3\text{C}_2\text{T}_x$ MXene: An Interstratification Process with Major Implications on Physical Properties. *Chem. Mater.* **2019**, *31*, 454–461. [[CrossRef](#)]
114. Dai, J.; Zhang, T.; Qi, R.; Zhao, H.; Fei, T.; Lu, G. LiCl Loaded Cross-Linked Polymer Composites by Click Reaction for Humidity Sensing. *Sens. Actuators B Chem.* **2017**, *253*, 361–367. [[CrossRef](#)]
115. Zhang, Z.; Huang, J.; Dong, B.; Yuan, Q.; He, Y.; Wolfbeis, O.S. Rational Tailoring of $\text{ZnSnO}_3/\text{TiO}_2$ Heterojunctions with Bioinspired Surface Wettability for High-Performance Humidity Nanosensors. *Nanoscale* **2015**, *7*, 4149–4155. [[CrossRef](#)] [[PubMed](#)]
116. Muckley, E.S.; Naguib, M.; Ivanov, I.N. Multi-Modal, Ultrasensitive, Wide-Range Humidity Sensing with Ti_3C_2 Film. *Nanoscale* **2018**, *10*, 21689–21695. [[CrossRef](#)]
117. Wu, J.; Lu, P.; Dai, J.; Zheng, C.; Zhang, T.; Yu, W.W.; Zhang, Y. High Performance Humidity Sensing Property of $\text{Ti}_3\text{C}_2\text{T}_x$ MXene-Derived $\text{Ti}_3\text{C}_2\text{T}_x/\text{K}_2\text{Ti}_4\text{O}_9$ Composites. *Sens. Actuators B Chem.* **2021**, *326*, 128969. [[CrossRef](#)]
118. An, H.; Habib, T.; Shah, S.; Gao, H.; Patel, A.; Echols, I.; Zhao, X.; Radovic, M.; Green, M.J.; Lutkenhaus, J.L. Water Sorption in MXene/Polyelectrolyte Multilayers for Ultrafast Humidity Sensing. *ACS Appl. Nano Mater.* **2019**, *2*, 948–955. [[CrossRef](#)]
119. Lu, Y.; Wang, M.-Y.; Wang, D.-Y.; Sun, Y.-H.; Liu, Z.-H.; Gao, R.-K.; Yu, L.-D.; Zhang, D.-Z. Flexible Impedance Sensor Based on $\text{Ti}_3\text{C}_2\text{T}_x$ MXene and Graphitic Carbon Nitride Nanohybrid for Humidity-Sensing Application with Ultrahigh Response. *Rare Met.* **2023**, *42*, 2204–2213. [[CrossRef](#)]
120. Han, M.; Shen, W. Nacre-Inspired Cellulose Nanofiber/MXene Flexible Composite Film with Mechanical Robustness for Humidity Sensing. *Carbohydr. Polym.* **2022**, *298*, 120109. [[CrossRef](#)]
121. Li, R.; Fan, Y.; Ma, Z.; Zhang, D.; Liu, Y.; Xu, J. Controllable Preparation of Ultrathin MXene Nanosheets and Their Excellent QCM Humidity Sensing Properties Enhanced by Fluoride Doping. *Microchim. Acta* **2021**, *188*, 81. [[CrossRef](#)]
122. Muckley, E.S.; Naguib, M.; Wang, H.-W.; Vlcek, L.; Osti, N.C.; Sacci, R.L.; Sang, X.; Unocic, R.R.; Xie, Y.; Tyagi, M.; et al. Multimodality of Structural, Electrical, and Gravimetric Responses of Intercalated MXenes to Water. *ACS Nano* **2017**, *11*, 11118–11126. [[CrossRef](#)]
123. Li, N.; Jiang, Y.; Xiao, Y.; Meng, B.; Xing, C.; Zhang, H.; Peng, Z. A Fully Inkjet-Printed Transparent Humidity Sensor Based on a $\text{Ti}_3\text{C}_2/\text{Ag}$ Hybrid for Touchless Sensing of Finger Motion. *Nanoscale* **2019**, *11*, 21522–21531. [[CrossRef](#)]
124. Sun, B.; Lv, H.; Liu, Z.; Wang, J.; Bai, X.; Zhang, Y.; Chen, J.; Kan, K.; Shi, K. $\text{Co}_3\text{O}_4/\text{PEI}/\text{Ti}_3\text{C}_2\text{T}_x$ MXene Nanocomposites for a Highly Sensitive NO_x Gas Sensor with a Low Detection Limit. *J. Mater. Chem. A Mater.* **2021**, *9*, 6335–6344. [[CrossRef](#)]

125. Kim, S.J.; Koh, H.-J.; Ren, C.E.; Kwon, O.; Maleski, K.; Cho, S.-Y.; Anasori, B.; Kim, C.-K.; Choi, Y.-K.; Kim, J.; et al. Metallic Ti₃C₂T_x MXene Gas Sensors with Ultrahigh Signal-to-Noise Ratio. *ACS Nano* **2018**, *12*, 986–993. [[CrossRef](#)]
126. John, R.A.B.; Vijayan, K.; Septiani, N.L.W.; Hardiansyah, A.; Kumar, A.R.; Yulianto, B.; Hermawan, A. Gas-Sensing Mechanisms and Performances of MXenes and MXene-Based Heterostructures. *Sensors* **2023**, *23*, 8674. [[CrossRef](#)]
127. Lee, E.; VahidMohammadi, A.; Prorok, B.C.; Yoon, Y.S.; Beidaghi, M.; Kim, D.-J. Room Temperature Gas Sensing of Two-Dimensional Titanium Carbide (MXene). *ACS Appl. Mater. Interfaces* **2017**, *9*, 37184–37190. [[CrossRef](#)] [[PubMed](#)]
128. Wu, M.; He, M.; Hu, Q.; Wu, Q.; Sun, G.; Xie, L.; Zhang, Z.; Zhu, Z.; Zhou, A. Ti₃C₂ MXene-Based Sensors with High Selectivity for NH₃ Detection at Room Temperature. *ACS Sens.* **2019**, *4*, 2763–2770. [[CrossRef](#)]
129. Lee, S.H.; Eom, W.; Shin, H.; Ambade, R.B.; Bang, J.H.; Kim, H.W.; Han, T.H. Room-Temperature, Highly Durable Ti₃C₂T_x MXene/Graphene Hybrid Fibers for NH₃ Gas Sensing. *ACS Appl. Mater. Interfaces* **2020**, *12*, 10434–10442. [[CrossRef](#)] [[PubMed](#)]
130. Shuvo, S.N.; Ulloa Gomez, A.M.; Mishra, A.; Chen, W.Y.; Dongare, A.M.; Stanciu, L.A. Sulfur-Doped Titanium Carbide MXenes for Room-Temperature Gas Sensing. *ACS Sens.* **2020**, *5*, 2915–2924. [[CrossRef](#)] [[PubMed](#)]
131. Bhardwaj, R.; Hazra, A. MXene-Based Gas Sensors. *J. Mater. Chem. C Mater.* **2021**, *9*, 15735–15754. [[CrossRef](#)]
132. Ismail, A.H.; Mohd Yahya, N.A.; Mahdi, M.A.; Yaacob, M.H.; Sulaiman, Y. Gasochromic Response of Optical Sensing Platform Integrated with Polyaniline and Poly(3,4-Ethylenedioxythiophene) Exposed to NH₃ Gas. *Polymer* **2020**, *192*, 122313. [[CrossRef](#)]
133. Ahamad, T.; Naushad, M.; Alshheri, S.M. Fabrication of Highly Porous N/S Doped Carbon Embedded with CuO/CuS Nanoparticles for NH₃ Gas Sensing. *Mater. Lett.* **2020**, *268*, 127515. [[CrossRef](#)]
134. Li, P.; Wang, B.; Qin, C.; Han, C.; Sun, L.; Wang, Y. Band-Gap-Tunable CeO₂ Nanoparticles for Room-Temperature NH₃ Gas Sensors. *Ceram. Int.* **2020**, *46*, 19232–19240. [[CrossRef](#)]
135. Liu, M.; Ji, J.; Song, P.; Wang, J.; Wang, Q. Sensing Performance of α -Fe₂O₃/Ti₃C₂T_x MXene Nanocomposites to NH₃ at Room Temperature. *J. Alloys Compd.* **2022**, *898*, 162812. [[CrossRef](#)]
136. Xiao, B.; Li, Y.-C.; Yu, X.F.; Cheng, J. MXenes: Reusable Materials for NH₃ Sensor or Capturer by Controlling the Charge Injection. *Sens. Actuators B Chem.* **2016**, *235*, 103–109. [[CrossRef](#)]
137. Kim, S.J.; Choi, J.; Maleski, K.; Hantanasirisakul, K.; Jung, H.-T.; Gogotsi, Y.; Ahn, C.W. Interfacial Assembly of Ultrathin, Functional MXene Films. *ACS Appl. Mater. Interfaces* **2019**, *11*, 32320–32327. [[CrossRef](#)]
138. Seekaew, Y.; Kamlue, S.; Wongchoosuk, C. Room-Temperature Ammonia Gas Sensor Based on Ti₃C₂T_x MXene/Graphene Oxide/CuO/ZnO Nanocomposite. *ACS Appl. Nano Mater.* **2023**, *6*, 9008–9020. [[CrossRef](#)]
139. Gabriunaite, I.; Valiuniene, A.; Ramanavicius, S.; Ramanavicius, A. Biosensors Based on Bio-Functionalized Semiconducting Metal Oxides. *Crit. Rev. Anal. Chem.* **2022**, 1–16. [[CrossRef](#)]
140. Celiesiute, R.; Ramanaviciene, A.; Gicevicius, M.; Ramanavicius, A. Electrochromic Sensors Based on Conducting Polymers, Metal Oxides, and Coordination Complexes. *Crit. Rev. Anal. Chem.* **2019**, *49*, 195–208. [[CrossRef](#)]
141. Ramanavicius, S.; Jagminas, A.; Ramanavicius, A. Gas Sensors Based on Titanium Oxides (Review). *Coatings* **2022**, *12*, 699. [[CrossRef](#)]
142. Ramanavicius, S.; Ramanavicius, A. Insights in the Application of Stoichiometric and Non-Stoichiometric Titanium Oxides for the Design of Sensors for the Determination of Gases and VOCs (TiO_{2-x} and TiO_{2n-1} vs. TiO₂). *Sensors* **2020**, *20*, 6833. [[CrossRef](#)]
143. Ramanavicius, S.; Tereshchenko, A.; Karpicz, R.; Ratautaite, V.; Bubniene, U.; Maneikis, A.; Jagminas, A.; Ramanavicius, A. TiO_{2-x}/TiO₂-Structure Based ‘Self-Heated’ Sensor for the Determination of Some Reducing Gases. *Sensors* **2020**, *20*, 74. [[CrossRef](#)] [[PubMed](#)]
144. Petruleviciene, M.; Savickaja, I.; Juodkazyte, J.; Ramanavicius, A. Investigation of WO₃ and BiVO₄ Photoanodes for Photoelectrochemical Sensing of Xylene, Toluene and Methanol. *Chemosensors* **2023**, *11*, 552. [[CrossRef](#)]
145. Ramanavičius, S.; Petrulevičienė, M.; Juodkazytė, J.; Grigucevičienė, A.; Ramanavičius, A. Selectivity of Tungsten Oxide Synthesized by Sol-Gel Method Towards Some Volatile Organic Compounds and Gaseous Materials in a Broad Range of Temperatures. *Materials* **2020**, *13*, 523. [[CrossRef](#)] [[PubMed](#)]
146. Petruleviciene, M.; Juodkazyte, J.; Parvin, M.; Tereshchenko, A.; Ramanavicius, S.; Karpicz, R.; Samukaite-Bubniene, U.; Ramanavicius, A. Tuning the Photo-Luminescence Properties of WO₃ Layers by the Adjustment of Layer Formation Conditions. *Materials* **2020**, *13*, 2814. [[CrossRef](#)] [[PubMed](#)]
147. Liu, M.; Wang, J.; Song, P.; Ji, J.; Wang, Q. Metal-Organic Frameworks-Derived In₂O₃ Microtubes/Ti₃C₂T_x MXene Composites for NH₃ Detection at Room Temperature. *Sens. Actuators B Chem.* **2022**, *361*, 131755. [[CrossRef](#)]
148. Pasupuleti, K.S.; Thomas, A.M.; Vidyasagar, D.; Rao, V.N.; Yoon, S.-G.; Kim, Y.-H.; Kim, S.-G.; Kim, M.-D. ZnO@Ti₃C₂T_x MXene Hybrid Composite-Based Schottky-Barrier-Coated SAW Sensor for Effective Detection of Sub-Ppb-Level NH₃ at Room Temperature under UV Illumination. *ACS Mater. Lett.* **2023**, *5*, 2739–2746. [[CrossRef](#)]
149. Liu, M.; Sun, R.-Y.; Ding, Y.-L.; Wang, Q.; Song, P. Au/ α -Fe₂O₃/Ti₃C₂T_x MXene Nanosheet Heterojunctions for High-Performance NH₃ Gas Detection at Room Temperature. *ACS Appl. Nano Mater.* **2023**, *6*, 11856–11867. [[CrossRef](#)]
150. Turemis, M.; Zappi, D.; Giardi, M.T.; Basile, G.; Ramanaviciene, A.; Kapralovs, A.; Ramanavicius, A.; Viter, R. ZnO/Polyaniline Composite Based Photoluminescence Sensor for the Determination of Acetic Acid Vapor. *Talanta* **2020**, *211*, 120658. [[CrossRef](#)]
151. Ramanavicius, S.; Ramanavicius, A. Conducting Polymers in the Design of Biosensors and Biofuel Cells. *Polymers* **2021**, *13*, 49. [[CrossRef](#)]
152. Ramanavicius, S.; Ramanavicius, A. Charge Transfer and Biocompatibility Aspects in Conducting Polymer-Based Enzymatic Biosensors and Biofuel Cells. *Nanomaterials* **2021**, *11*, 371. [[CrossRef](#)] [[PubMed](#)]

153. Gicevicius, M.; Celiesiute, R.; Kucinski, J.; Ramanaviciene, A.; Bagdziunas, G.; Ramanavicius, A. Analytical Evaluation of Optical PH-Sensitivity of Polyaniline Layer Electrochemically Deposited on ITO Electrode. *J. Electrochem. Soc.* **2018**, *165*, H903. [[CrossRef](#)]
154. Ramanavicius, S.; Jagminas, A.; Ramanavicius, A. Advances in Molecularly Imprinted Polymers Based Affinity Sensors (Review). *Polymers* **2021**, *13*, 974. [[CrossRef](#)] [[PubMed](#)]
155. Gicevicius, M.; Kucinski, J.; Ramanaviciene, A.; Ramanavicius, A. Tuning the Optical PH Sensing Properties of Polyaniline-Based Layer by Electrochemical Copolymerization of Aniline with o-Phenylenediamine. *Dye. Pigment.* **2019**, *170*, 107457. [[CrossRef](#)]
156. Ramanavicius, S.; Samukaite-Bubniene, U.; Ratautaite, V.; Bechelany, M.; Ramanavicius, A. Electrochemical Molecularly Imprinted Polymer Based Sensors for Pharmaceutical and Biomedical Applications (Review). *J. Pharm. Biomed. Anal.* **2022**, *215*, 114739. [[CrossRef](#)]
157. Ramanavicius, S.; Ramanavicius, A. Development of Molecularly Imprinted Polymer Based Phase Boundaries for Sensors Design (Review). *Adv. Colloid. Interface Sci.* **2022**, *305*, 102693. [[CrossRef](#)]
158. Jin, L.; Wu, C.; Wei, K.; He, L.; Gao, H.; Zhang, H.; Zhang, K.; Asiri, A.M.; Alamry, K.A.; Yang, L.; et al. Polymeric Ti₃C₂T_x MXene Composites for Room Temperature Ammonia Sensing. *ACS Appl. Nano Mater.* **2020**, *3*, 12071–12079. [[CrossRef](#)]
159. Wang, X.; Zhang, D.; Zhang, H.; Gong, L.; Yang, Y.; Zhao, W.; Yu, S.; Yin, Y.; Sun, D. In Situ Polymerized Polyaniline/MXene (V₂C) as Building Blocks of Supercapacitor and Ammonia Sensor Self-Powered by Electromagnetic-Triboelectric Hybrid Generator. *Nano Energy* **2021**, *88*, 106242. [[CrossRef](#)]
160. Li, X.; Wang, H.; Li, H.; Chen, Y.; Ni, Y.; Xia, Y. Zr₃C₂O₂ MXene as Promising Candidate for NH₃ Sensor with High Sensitivity and Selectivity at Room Temperature. *Appl. Surf. Sci.* **2023**, *624*, 157125. [[CrossRef](#)]
161. Gao, X.; Zhang, T. An Overview: Facet-Dependent Metal Oxide Semiconductor Gas Sensors. *Sens. Actuators B Chem.* **2018**, *277*, 604–633. [[CrossRef](#)]
162. Zhang, D.; Wu, Z.; Zong, X. Flexible and Highly Sensitive H₂S Gas Sensor Based on In-Situ Polymerized SNO₂/RGO/PANI Ternary Nanocomposite with Application in Halitosis Diagnosis. *Sens. Actuators B Chem.* **2019**, *289*, 32–41. [[CrossRef](#)]
163. Gui, Y.; Yang, L.; Tian, K.; Zhang, H.; Fang, S. P-Type Co₃O₄ Nanoarrays Decorated on the Surface of n-Type Flower-like WO₃ Nanosheets for High-Performance Gas Sensing. *Sens. Actuators B Chem.* **2019**, *288*, 104–112. [[CrossRef](#)]
164. Xu, Y.; Ma, T.; Zheng, L.; Zhao, Y.; Liu, X.; Zhang, J. Heterostructures of Hematite-Sensitized W₁₈O₄₉ Hollow Spheres for Improved Acetone Detection with Ultralow Detection Limit. *Sens. Actuators B Chem.* **2019**, *288*, 432–441. [[CrossRef](#)]
165. Zhang, R.; Zhou, T.; Wang, L.; Zhang, T. Metal–Organic Frameworks-Derived Hierarchical Co₃O₄ Structures as Efficient Sensing Materials for Acetone Detection. *ACS Appl. Mater. Interfaces* **2018**, *10*, 9765–9773. [[CrossRef](#)]
166. Wang, Z.; Wang, C. Is Breath Acetone a Biomarker of Diabetes? A Historical Review on Breath Acetone Measurements. *J. Breath. Res.* **2013**, *7*, 037109. [[CrossRef](#)] [[PubMed](#)]
167. Sun, S.; Wang, M.; Chang, X.; Jiang, Y.; Zhang, D.; Wang, D.; Zhang, Y.; Lei, Y. W₁₈O₄₉/Ti₃C₂T_x Mxene Nanocomposites for Highly Sensitive Acetone Gas Sensor with Low Detection Limit. *Sens. Actuators B Chem.* **2020**, *304*, 127274. [[CrossRef](#)]
168. Liu, M.; Wang, Z.; Song, P.; Yang, Z.; Wang, Q. Flexible MXene/RGO/CuO Hybrid Aerogels for High Performance Acetone Sensing at Room Temperature. *Sens. Actuators B Chem.* **2021**, *340*, 129946. [[CrossRef](#)]
169. Majhi, S.M.; Ali, A.; Greish, Y.E.; El-Maghraby, H.F.; Mahmoud, S.T. V₂CT_x MXene-Based Hybrid Sensor with High Selectivity and Ppb-Level Detection for Acetone at Room Temperature. *Sci. Rep.* **2023**, *13*, 3114. [[CrossRef](#)] [[PubMed](#)]
170. Zhao, X.; Zhang, G.; Wang, J.; Yuan, T.; Huang, J.; Wang, L.; Liu, Y.-N. Ru Nanoclusters Supported on Ti₃C₂T_x Nanosheets for Catalytic Hydrogenation of Quinolines. *ACS Appl. Nano Mater.* **2022**, *5*, 6213–6220. [[CrossRef](#)]
171. Lee, J.T.; Wyatt, B.C.; Davis, G.A., Jr.; Masterson, A.N.; Pagan, A.L.; Shah, A.; Anasori, B.; Sardar, R. Covalent Surface Modification of Ti₃C₂T_x MXene with Chemically Active Polymeric Ligands Producing Highly Conductive and Ordered Microstructure Films. *ACS Nano* **2021**, *15*, 19600–19612. [[CrossRef](#)] [[PubMed](#)]
172. Hermawan, A.; Zhang, B.; Taufik, A.; Asakura, Y.; Hasegawa, T.; Zhu, J.; Shi, P.; Yin, S. CuO Nanoparticles/Ti₃C₂T_x MXene Hybrid Nanocomposites for Detection of Toluene Gas. *ACS Appl. Nano Mater.* **2020**, *3*, 4755–4766. [[CrossRef](#)]
173. Guo, W.; Surya, S.G.; Babar, V.; Ming, F.; Sharma, S.; Alshareef, H.N.; Schwingenschlög, U.; Salama, K.N. Selective Toluene Detection with Mo₂CT_x MXene at Room Temperature. *ACS Appl. Mater. Interfaces* **2020**, *12*, 57218–57227. [[CrossRef](#)]
174. Park, H.J.; Hong, S.Y.; Chun, D.H.; Kang, S.W.; Park, J.C.; Lee, D.-S. A Highly Susceptive Mesoporous Hematite Microcube Architecture for Sustainable P-Type Formaldehyde Gas Sensors. *Sens. Actuators B Chem.* **2019**, *287*, 437–444. [[CrossRef](#)]
175. Fu, X.; Yang, P.; Xiao, X.; Zhou, D.; Huang, R.; Zhang, X.; Cao, F.; Xiong, J.; Hu, Y.; Tu, Y.; et al. Ultra-Fast and Highly Selective Room-Temperature Formaldehyde Gas Sensing of Pt-Decorated MoO₃ Nanobelts. *J. Alloys Compd.* **2019**, *797*, 666–675. [[CrossRef](#)]
176. Zhao, R.; Zhang, X.; Peng, S.; Hong, P.; Zou, T.; Wang, Z.; Xing, X.; Yang, Y.; Wang, Y. Shaddock Peels as Bio-Templates Synthesis of Cd-Doped SnO₂ Nanofibers: A High Performance Formaldehyde Sensing Material. *J. Alloys Compd.* **2020**, *813*, 152170. [[CrossRef](#)]
177. Shuaishuai, J.; Wan, X.; Cuimin, Z.; Feihu, L.; Bo, M.; Zili, Z. Improving the Formaldehyde Gas Sensing Performance of the ZnO/SnO₂ Nanoparticles by PdO Decoration. *J. Mater. Sci. Mater. Electron.* **2020**, *31*, 684–692. [[CrossRef](#)]
178. Chen, X.; Shen, Y.; Zhou, P.; Zhao, S.; Zhong, X.; Li, T.; Han, C.; Wei, D.; Meng, D. NO₂ Sensing Properties of One-Pot-Synthesized ZnO Nanowires with Pd Functionalization. *Sens. Actuators B Chem.* **2019**, *280*, 151–161. [[CrossRef](#)]
179. Zhang, D.; Mi, Q.; Wang, D.; Li, T. MXene/Co₃O₄ Composite Based Formaldehyde Sensor Driven by ZnO/MXene Nanowire Arrays Piezoelectric Nanogenerator. *Sens. Actuators B Chem.* **2021**, *339*, 129923. [[CrossRef](#)]
180. Niu, G.; Zhang, M.; Wu, B.; Zhuang, Y.; Ramachandran, R.; Zhao, C.; Wang, F. Nanocomposites of Pre-Oxidized Ti₃C₂T_x MXene and SnO₂ Nanosheets for Highly Sensitive and Stable Formaldehyde Gas Sensor. *Ceram. Int.* **2023**, *49*, 2583–2590. [[CrossRef](#)]

181. Mirzaei, A.; Leonardi, S.G.; Neri, G. Detection of Hazardous Volatile Organic Compounds (VOCs) by Metal Oxide Nanostructures-Based Gas Sensors: A Review. *Ceram. Int.* **2016**, *42*, 15119–15141. [[CrossRef](#)]
182. Wang, X.; Sun, K.; Li, K.; Li, X.; Gogotsi, Y. $\text{Ti}_3\text{C}_2\text{T}_x$ /PEDOT:PSS Hybrid Materials for Room-Temperature Methanol Sensor. *Chin. Chem. Lett.* **2020**, *31*, 1018–1021. [[CrossRef](#)]
183. Liu, M.; Wang, Z.; Song, P.; Yang, Z.; Wang, Q. In_2O_3 Nanocubes/ $\text{Ti}_3\text{C}_2\text{T}_x$ MXene Composites for Enhanced Methanol Gas Sensing Properties at Room Temperature. *Ceram. Int.* **2021**, *47*, 23028–23037. [[CrossRef](#)]
184. Jiang, B.; Lu, J.; Han, W.; Sun, Y.; Wang, Y.; Cheng, P.; Zhang, H.; Wang, C.; Lu, G. Hierarchical Mesoporous Zinc Oxide Microspheres for Ethanol Gas Sensor. *Sens. Actuators B Chem.* **2022**, *357*, 131333. [[CrossRef](#)]
185. Zhang, J.; Ma, S.; Wang, B.; Pei, S. Hydrothermal Synthesis of SnO_2 -CuO Composite Nanoparticles as a Fast-Response Ethanol Gas Sensor. *J. Alloys Compd.* **2021**, *886*, 161299. [[CrossRef](#)]
186. Sharma, B.; Karuppasamy, K.; Vikraman, D.; Jo, E.-B.; Sivakumar, P.; Kim, H.-S. Porous, 3D-Hierarchical α -NiMoO₄ Rectangular Nanosheets for Selective Conductometric Ethanol Gas Sensors. *Sens. Actuators B Chem.* **2021**, *347*, 130615. [[CrossRef](#)]
187. Tseng, S.-F.; Chen, C.-W. Synthesis of Nanograined SnO_2 Films on Laser-Patterned Graphene/Ceramic Substrates for Low-Temperature Ethanol Gas Sensors. *Ceram. Int.* **2021**, *47*, 33498–33508. [[CrossRef](#)]
188. Mao, J.N.; Hong, B.; Chen, H.D.; Gao, M.H.; Xu, J.C.; Han, Y.B.; Yang, Y.T.; Jin, H.X.; Jin, D.F.; Peng, X.L.; et al. Highly Improved Ethanol Gas Response of N-Type α -Fe₂O₃ Bunched Nanowires Sensor with High-Valence Donor-Doping. *J. Alloys Compd.* **2020**, *827*, 154248. [[CrossRef](#)]
189. Zhang, S.; Song, P.; Sun, J.; Ding, Y.; Wang, Q. MoO_3 / $\text{Ti}_3\text{C}_2\text{T}_x$ MXene Nanocomposites with Rapid Response for Enhanced Ethanol-Sensing at a Low Temperature. *Sens. Actuators B Chem.* **2023**, *378*, 133216. [[CrossRef](#)]
190. Wang, C.; Li, R.; Feng, L.; Xu, J. The SnO_2 /MXene Composite Ethanol Sensor Based on MEMS Platform. *Chemosensors* **2022**, *10*, 109. [[CrossRef](#)]
191. Ai, T.; Li, J.; Nie, S.; Yin, Y.; Lu, J.; Bao, S.; Yan, L. High-Performance H₂ Gas Sensor Based on Mn-Doped α -Fe₂O₃ Polyhedrons from N, N-Dimethylformamide Assisted Hydrothermal Synthesis. *Int. J. Hydrogen Energy* **2022**, *47*, 20561–20571. [[CrossRef](#)]
192. Long, Y.; Xu, H.; He, J.; Li, C.; Zhu, M. Piezoelectric Polarization of BiOCl via Capturing Mechanical Energy for Catalytic H₂ Evolution. *Surf. Interfaces* **2022**, *31*, 102056. [[CrossRef](#)]
193. Meng, X.; Bi, M.; Xiao, Q.; Gao, W. Ultrasensitive Gas Sensor Based on Pd/SnS₂/SnO₂ Nanocomposites for Rapid Detection of H₂. *Sens. Actuators B Chem.* **2022**, *359*, 131612. [[CrossRef](#)]
194. Zhu, S.; Tian, Q.; Wu, G.; Bian, W.; Sun, N.; Wang, X.; Li, C.; Zhang, Y.; Dou, H.; Gong, C.; et al. Highly Sensitive and Stable H₂ Gas Sensor Based on P-PdO-n-WO₃-Heterostructure-Homogeneously-Dispersing Thin Film. *Int. J. Hydrogen Energy* **2022**, *47*, 17821–17834. [[CrossRef](#)]
195. Wang, L.; Xiao, Z.; Yao, X.; Yu, X.; Tu, S.-T.; Chen, S. Pt=Pd Separation Modified $\text{Ti}_3\text{C}_2\text{T}_x$ MXene for Hydrogen Detection at Room Temperature. *Int. J. Hydrogen Energy* **2023**, *48*, 30205–30217. [[CrossRef](#)]
196. Xia, Y.; Zhou, L.; Yang, J.; Du, P.; Xu, L.; Wang, J. Highly Sensitive and Fast Optoelectronic Room-Temperature NO₂ Gas Sensor Based on ZnO Nanorod-Assembled Macro-/Mesoporous Film. *ACS Appl. Electron. Mater.* **2020**, *2*, 580–589. [[CrossRef](#)]
197. Guo, F.; Feng, C.; Zhang, Z.; Zhang, L.; Xu, C.; Zhang, C.; Lin, S.; Wu, H.; Zhang, B.; Tabusi, A.; et al. A Room-Temperature NO₂ Sensor Based on $\text{Ti}_3\text{C}_2\text{T}_x$ MXene Modified with Sphere-like CuO. *Sens. Actuators B Chem.* **2023**, *375*, 132885. [[CrossRef](#)]
198. Gasso, S.; Kaur Sohal, M.; Chand Singh, R.; Mahajan, A. NO_x Sensor Based on Semiconductor Metal Oxide and MXene Nanostructures. *Mater. Today Proc.* **2023**, *92*, 632–635. [[CrossRef](#)]
199. Sun, B.; Qin, F.; Jiang, L.; Gao, J.; Liu, Z.; Wang, J.; Zhang, Y.; Fan, J.; Kan, K.; Shi, K. Room-Temperature Gas Sensors Based on Three-Dimensional Co_3O_4 /Al₂O₃@ $\text{Ti}_3\text{C}_2\text{T}_x$ MXene Nanocomposite for Highly Sensitive NO_x Detection. *Sens. Actuators B Chem.* **2022**, *368*, 132206. [[CrossRef](#)]
200. Kuang, D.; Wang, L.; Guo, X.; She, Y.; Du, B.; Liang, C.; Qu, W.; Sun, X.; Wu, Z.; Hu, W.; et al. Facile Hydrothermal Synthesis of $\text{Ti}_3\text{C}_2\text{T}_x$ -TiO₂ Nanocomposites for Gaseous Volatile Organic Compounds Detection at Room Temperature. *J. Hazard. Mater.* **2021**, *416*, 126171. [[CrossRef](#)]
201. Zhou, Y.; Wang, Y.; Wang, Y.; Li, X. Humidity-Enabled Ionic Conductive Trace Carbon Dioxide Sensing of Nitrogen-Doped $\text{Ti}_3\text{C}_2\text{T}_x$ MXene/Polyethyleneimine Composite Films Decorated with Reduced Graphene Oxide Nanosheets. *Anal. Chem.* **2020**, *92*, 16033–16042. [[CrossRef](#)] [[PubMed](#)]
202. Wang, J.; Xu, R.; Xia, Y.; Komarneni, S. Ti_2CT_x MXene: A Novel p-Type Sensing Material for Visible Light-Enhanced Room Temperature Methane Detection. *Ceram. Int.* **2021**, *47*, 34437–34442. [[CrossRef](#)]
203. Persson, P.; Rosen, J. Current State of the Art on Tailoring the MXene Composition, Structure, and Surface Chemistry. *Curr. Opin. Solid. State Mater. Sci.* **2019**, *23*, 100774. [[CrossRef](#)]
204. Rhouati, A.; Berkani, M.; Vasseghian, Y.; Golzadeh, N. MXene-Based Electrochemical Sensors for Detection of Environmental Pollutants: A Comprehensive Review. *Chemosphere* **2022**, *291*, 132921. [[CrossRef](#)]
205. Park, Y.J.; Peñas-Defrutos, M.N.; Drummond, M.J.; Gordon, Z.; Kelly, O.R.; Garvey, I.J.; Gullett, K.L.; García-Melchor, M.; Fout, A.R. Secondary Coordination Sphere Influences the Formation of Fe(III)-O or Fe(III)-OH in Nitrite Reduction: A Synthetic and Computational Study. *Inorg. Chem.* **2022**, *61*, 8182–8192. [[CrossRef](#)]
206. Hao, D.; Liu, Y.; Gao, S.; Arandiyani, H.; Bai, X.; Kong, Q.; Wei, W.; Shen, P.K.; Ni, B.-J. Emerging Artificial Nitrogen Cycle Processes through Novel Electrochemical and Photochemical Synthesis. *Mater. Today* **2021**, *46*, 212–233. [[CrossRef](#)]

207. Hou, C.-Y.; Fu, L.-M.; Ju, W.-J.; Wu, P.-Y. Microfluidic Colorimetric System for Nitrite Detection in Foods. *Chem. Eng. J.* **2020**, *398*, 125573. [[CrossRef](#)]
208. Guadagnini, L.; Tonelli, D. Carbon Electrodes Unmodified and Decorated with Silver Nanoparticles for the Determination of Nitrite, Nitrate and Iodate. *Sens. Actuators B Chem.* **2013**, *188*, 806–814. [[CrossRef](#)]
209. Wang, T.; Wang, C.; Xu, X.; Li, Z.; Li, D. One-Step Electrodeposition Synthesized Aunps/Mxene/ERGO for Selectivity Nitrite Sensing. *Nanomaterials* **2021**, *11*, 1892. [[CrossRef](#)]
210. Wang, Y.; Zeng, Z.; Qiao, J.; Dong, S.; Liang, Q.; Shao, S. Ultrasensitive Determination of Nitrite Based on Electrochemical Platform of AuNPs Deposited on PDDA-Modified MXene Nanosheets. *Talanta* **2021**, *221*, 121605. [[CrossRef](#)]
211. Feng, X.; Han, G.; Cai, J.; Wang, X. Au@Carbon Quantum Dots-MXene Nanocomposite as an Electrochemical Sensor for Sensitive Detection of Nitrite. *J. Colloid. Interface Sci.* **2022**, *607*, 1313–1322. [[CrossRef](#)]
212. Zhuang, J.; Pan, H.; Feng, W. 3D Urchin-like CoVO/MXene Nanosheet Composites for Enhanced Detection Signal of Nitrite. *Sens. Actuators B Chem.* **2023**, *378*, 133207. [[CrossRef](#)]
213. Schmidt, E.W. *Hydrazine and Its Derivatives: Preparation, Properties, Applications, 2 Volume Set*; John Wiley & Sons: Hoboken, NJ, USA, 2001; ISBN 0471415537.
214. Mackinson, F.W. Occupational Health Guidelines for Chemical Hazards. *NIOSH OSHA* **1981**, *4*, 81–123.
215. Soundiraraju, B.; Raghavan, R.; George, B.K. Chromium Carbide Nanosheets Prepared by Selective Etching of Aluminum from Cr₂AlC for Hydrazine Detection. *ACS Appl. Nano Mater.* **2020**, *3*, 11007–11016. [[CrossRef](#)]
216. Soundiraraju, B.; Anthony, A.M.; Pandurangan, P.; George, B.K. Electrochemical Behavior of Chromium Carbide MXene Modified Electrodes: Hydrazine Sensing. *Mater. Today Commun.* **2022**, *32*, 103982. [[CrossRef](#)]
217. Yao, Y.; Han, X.; Yang, X.; Zhao, J.; Chai, C. Detection of Hydrazine at MXene/ZIF-8 Nanocomposite Modified Electrode. *Chin. J. Chem.* **2021**, *39*, 330–336. [[CrossRef](#)]
218. Gul, S.; Serna, M.I.; Zahra, S.A.; Arif, N.; Iqbal, M.; Akinwande, D.; Rizwan, S. Un-Doped and Er-Adsorbed Layered Nb₂C MXene for Efficient Hydrazine Sensing Application. *Surf. Interfaces* **2021**, *24*, 101074. [[CrossRef](#)]
219. Yang, H.; Li, S.; Yu, H.; Zheng, F.; Lin, L.; Chen, J.; Li, Y.; Lin, Y. In Situ Construction of Hollow Carbon Spheres with N, Co, and Fe Co-Doping as Electrochemical Sensors for Simultaneous Determination of Dihydroxybenzene Isomers. *Nanoscale* **2019**, *11*, 8950–8958. [[CrossRef](#)]
220. Shen, Y.; Rao, D.; Sheng, Q.; Zheng, J. Simultaneous Voltammetric Determination of Hydroquinone and Catechol by Using a Glassy Carbon Electrode Modified with Carboxy-Functionalized Carbon Nanotubes in a Chitosan Matrix and Decorated with Gold Nanoparticles. *Microchim. Acta* **2017**, *184*, 3591–3601. [[CrossRef](#)]
221. Wu, L.; Lu, X.; Dhanjai; Wu, Z.-S.; Dong, Y.; Wang, X.; Zheng, S.; Chen, J. 2D Transition Metal Carbide MXene as a Robust Biosensing Platform for Enzyme Immobilization and Ultrasensitive Detection of Phenol. *Biosens. Bioelectron.* **2018**, *107*, 69–75. [[CrossRef](#)]
222. Lei, L.; Li, C.; Huang, W.; Wu, K. Simultaneous Detection of 4-Chlorophenol and 4-Nitrophenol Using a Ti₃C₂T_x MXene Based Electrochemical Sensor. *Analyst* **2021**, *146*, 7593–7600. [[CrossRef](#)]
223. Krishnamoorthy, R.; Muthumalai, K.; Nagaraja, T.; Rajendrakumar, R.T.; Das, S.R. Chemically Exfoliated Titanium Carbide MXene for Highly Sensitive Electrochemical Sensors for Detection of 4-Nitrophenols in Drinking Water. *ACS Omega* **2022**, *7*, 42644–42654. [[CrossRef](#)] [[PubMed](#)]
224. Huang, R.; Liao, D.; Liu, Z.; Yu, J.; Jiang, X. Electrostatically Assembling 2D Hierarchical Nb₂CT_x and Zifs-Derivatives into Zn-Co-NC Nanocage for the Electrochemical Detection of 4-Nitrophenol. *Sens. Actuators B Chem.* **2021**, *338*, 129828. [[CrossRef](#)]
225. Rasheed, P.A.; Pandey, R.P.; Jabbar, K.A.; Mahmoud, K.A. Platinum Nanoparticles/Ti₃C₂T_x (MXene) Composite for the Effectual Electrochemical Sensing of Bisphenol A in Aqueous Media. *J. Electroanal. Chem.* **2021**, *880*, 114934. [[CrossRef](#)]
226. Huang, R.; Liao, D.; Chen, S.; Yu, J.; Jiang, X. A Strategy for Effective Electrochemical Detection of Hydroquinone and Catechol: Decoration of Alkalization-Intercalated Ti₃C₂ with MOF-Derived N-Doped Porous Carbon. *Sens. Actuators B Chem.* **2020**, *320*, 128386. [[CrossRef](#)]
227. Tu, X.; Gao, F.; Ma, X.; Zou, J.; Yu, Y.; Li, M.; Qu, F.; Huang, X.; Lu, L. Mxene/Carbon Nanohorn/ β -Cyclodextrin-Metal-Organic Frameworks as High-Performance Electrochemical Sensing Platform for Sensitive Detection of Carbendazim Pesticide. *J. Hazard. Mater.* **2020**, *396*, 122776. [[CrossRef](#)] [[PubMed](#)]
228. Xie, Y.; Gao, F.; Tu, X.; Ma, X.; Xu, Q.; Dai, R.; Huang, X.; Yu, Y.; Lu, L. Facile Synthesis of MXene/Electrochemically Reduced Graphene Oxide Composites and Their Application for Electrochemical Sensing of Carbendazim. *J. Electrochem. Soc.* **2019**, *166*, B1673. [[CrossRef](#)]
229. He, Y.; Zhou, X.; Zhou, L.; Zhang, X.; Ma, L.; Jiang, Y.; Gao, J. Self-Reducing Prussian Blue on Ti₃C₂T_x MXene Nanosheets as a Dual-Functional Nanohybrid for Hydrogen Peroxide and Pesticide Sensing. *Ind. Eng. Chem. Res.* **2020**, *59*, 15556–15564. [[CrossRef](#)]
230. Zhao, F.; Yao, Y.; Jiang, C.; Shao, Y.; Barceló, D.; Ying, Y.; Ping, J. Self-Reduction Bimetallic Nanoparticles on Ultrathin MXene Nanosheets as Functional Platform for Pesticide Sensing. *J. Hazard. Mater.* **2020**, *384*, 121358. [[CrossRef](#)]
231. Zhou, L.; Zhang, X.; Ma, L.; Gao, J.; Jiang, Y. Acetylcholinesterase/Chitosan-Transition Metal Carbides Nanocomposites-Based Biosensor for the Organophosphate Pesticides Detection. *Biochem. Eng. J.* **2017**, *128*, 243–249. [[CrossRef](#)]
232. Lin, C.; Song, X.; Ye, W.; Liu, T.; Rong, M.; Niu, L. Recent Progress in Optical Sensors Based on MXenes Quantum Dots and MXenes Nanosheets. *J. Anal. Test.* **2023**, *8*, 95–113. [[CrossRef](#)]

233. Wu, L.; Yuan, X.; Tang, Y.; Wageh, S.; Al-Hartomy, O.A.; Al-Sehemi, A.G.; Yang, J.; Xiang, Y.; Zhang, H.; Qin, Y. MXene Sensors Based on Optical and Electrical Sensing Signals: From Biological, Chemical, and Physical Sensing to Emerging Intelligent and Bionic Devices. *PhotoniX* **2023**, *4*, 15. [[CrossRef](#)]
234. Bhardwaj, S.K.; Singh, H.; Khatri, M.; Kim, K.-H.; Bhardwaj, N. Advances in MXenes-Based Optical Biosensors: A Review. *Biosens. Bioelectron.* **2022**, *202*, 113995. [[CrossRef](#)]
235. Chaudhuri, K.; Alhabeab, M.; Wang, Z.; Shalae, V.M.; Gogotsi, Y.; Boltasseva, A. Highly Broadband Absorber Using Plasmonic Titanium Carbide (MXene). *ACS Photonics* **2018**, *5*, 1115–1122. [[CrossRef](#)]
236. Li, R.; Zhang, L.; Shi, L.; Wang, P. MXene Ti₃C₂: An Effective 2D Light-to-Heat Conversion Material. *ACS Nano* **2017**, *11*, 3752–3759. [[CrossRef](#)]
237. Cui, Y.; Yang, K.; Zhang, F.; Lyu, Y.; Zhang, Q.; Zhang, B. Ultra-Light MXene/CNTs/PI Aerogel with Neat Arrangement for Electromagnetic Wave Absorption and Photothermal Conversion. *Compos. Part A Appl. Sci. Manuf.* **2022**, *158*, 106986. [[CrossRef](#)]
238. Li, W.; Miao, Y.; Zheng, Y.; Zhang, K.; Yao, J. Nb₂CT_x MXene Integrated Tapered Microfiber Based on Light-Controlled Light for Ultra-Sensitive and Wide-Range Hemoglobin Detection. *IEEE Sens. J.* **2022**, *22*, 11456–11462. [[CrossRef](#)]
239. Kumar, A.; Verma, P.; Jindal, P. Surface Plasmon Resonance Biosensor Based on a D-Shaped Photonic Crystal Fiber Using Ti₃C₂T_x MXene Material. *Opt. Mater.* **2022**, *128*, 112397. [[CrossRef](#)]
240. Ma, C.; Cao, Y.; Gou, X.; Zhu, J.-J. Recent Progress in Electrochemiluminescence Sensing and Imaging. *Anal. Chem.* **2020**, *92*, 431–454. [[CrossRef](#)]
241. Sojic, N. *Analytical Electrogenerated Chemiluminescence: From Fundamentals to Bioassays*; Royal Society of Chemistry: London, UK, 2019; Volume 15, ISBN 1788014146.
242. Ramanaviciene, A.; German, N.; Kausaite-Minkstimiene, A.; Voronovic, J.; Kirlyte, J.; Ramanavicius, A. Comparative Study of Surface Plasmon Resonance, Electrochemical and Electroassisted Chemiluminescence Methods Based Immunosensor for the Determination of Antibodies against Human Growth Hormone. *Biosens. Bioelectron.* **2012**, *36*, 48–55. [[CrossRef](#)]
243. Ma, X.; Gao, W.; Du, F.; Yuan, F.; Yu, J.; Guan, Y.; Sojic, N.; Xu, G. Rational Design of Electrochemiluminescent Devices. *ACC Chem. Res.* **2021**, *54*, 2936–2945. [[CrossRef](#)]
244. Kerr, E.; Farr, R.; Doeven, E.H.; Nai, Y.H.; Alexander, R.; Guijt, R.M.; Prieto-Simon, B.; Francis, P.S.; Dearnley, M.; Hayne, D.J.; et al. Amplification-Free Electrochemiluminescence Molecular Beacon-Based MicroRNA Sensing Using a Mobile Phone for Detection. *Sens. Actuators B Chem.* **2021**, *330*, 129261. [[CrossRef](#)]
245. Daley, G.Q.; Van Etten, R.A.; Baltimore, D. Induction of Chronic Myelogenous Leukemia in Mice by the P210^{bcr/Ab1} Gene of the Philadelphia Chromosome. *Science* **1990**, *247*, 824–830. [[CrossRef](#)]
246. Cheng, W.; Lin, Z.; Zhao, L.; Fan, N.; Bai, H.; Cheng, W.; Zhao, M.; Ding, S. CeO₂/MXene Heterojunction-Based Ultrasensitive Electrochemiluminescence Biosensing for BCR-ABL Fusion Gene Detection Combined with Dual-Toehold Strand Displacement Reaction for Signal Amplification. *Biosens. Bioelectron.* **2022**, *210*, 114287. [[CrossRef](#)]
247. Zhou, H.; Liu, J.; Xu, J.-J.; Zhang, S.; Chen, H.-Y. Chapter Two—Advances in DNA/RNA Detection Using Nanotechnology. In *Advances in Clinical Chemistry*; Makowski, G.S., Ed.; Elsevier: Amsterdam, The Netherlands, 2019; Volume 91, pp. 31–98, ISBN 0065-2423.
248. Viter, R.; Kunene, K.; Genys, P.; Jevdokimovs, D.; Erts, D.; Sutka, A.; Bisetty, K.; Viksna, A.; Ramanaviciene, A.; Ramanavicius, A. Photoelectrochemical Bisphenol S Sensor Based on ZnO-Nanoroads Modified by Molecularly Imprinted Polypyrrole. *Macromol. Chem. Phys.* **2020**, *221*, 1900232. [[CrossRef](#)]
249. Zhao, W.-W.; Xu, J.-J.; Chen, H.-Y. Photoelectrochemical Bioanalysis: The State of the Art. *Chem. Soc. Rev.* **2015**, *44*, 729–741. [[CrossRef](#)]
250. Zhou, Q.; Tang, D. Recent Advances in Photoelectrochemical Biosensors for Analysis of Mycotoxins in Food. *TrAC Trends Anal. Chem.* **2020**, *124*, 115814. [[CrossRef](#)]
251. Zhao, W.-W.; Xu, J.-J.; Chen, H.-Y. Photoelectrochemical DNA Biosensors. *Chem. Rev.* **2014**, *114*, 7421–7441. [[CrossRef](#)]
252. Liu, F.; Zhao, J.; Liu, X.; Zhen, X.; Feng, Q.; Gu, Y.; Yang, G.; Qu, L.; Zhu, J.-J. PEC-SERS Dual-Mode Detection of Foodborne Pathogens Based on Binding-Induced DNA Walker and C₃N₄/MXene-Au NPs Accelerator. *Anal. Chem.* **2023**, *95*, 14297–14307. [[CrossRef](#)]
253. Wang, L.; Zhu, F.; Chen, M.; Zhu, Y.; Xiao, J.; Yang, H.; Chen, X. Rapid and Visual Detection of Aflatoxin B1 in Foodstuffs Using Aptamer/G-Quadruplex DNAzyme Probe with Low Background Noise. *Food Chem.* **2019**, *271*, 581–587. [[CrossRef](#)] [[PubMed](#)]
254. Viter, R.; Savchuk, M.; Iatsunskyi, I.; Pietralik, Z.; Starodub, N.; Shpyrka, N.; Ramanaviciene, A.; Ramanavicius, A. Analytical, Thermodynamical and Kinetic Characteristics of Photoluminescence Immunosensor for the Determination of Ochratoxin A. *Biosens. Bioelectron.* **2018**, *99*, 237–243. [[CrossRef](#)]
255. Lu, X.; Wang, C.; Qian, J.; Ren, C.; An, K.; Wang, K. Target-Driven Switch-on Fluorescence Aptasensor for Trace Aflatoxin B1 Determination Based on Highly Fluorescent Ternary CdZnTe Quantum Dots. *Anal. Chim. Acta* **2019**, *1047*, 163–171. [[CrossRef](#)] [[PubMed](#)]
256. Wu, Z.; Sun, D.-W.; Pu, H.; Wei, Q. A Novel Fluorescence Biosensor Based on CRISPR/Cas12a Integrated MXenes for Detecting Aflatoxin B1. *Talanta* **2023**, *252*, 123773. [[CrossRef](#)]
257. Bandodkar, A.J.; Gutruf, P.; Choi, J.; Lee, K.; Sekine, Y.; Reeder, J.T.; Jeang, W.J.; Aranyosi, A.J.; Lee, S.P.; Model, J.B.; et al. Battery-Free, Skin-Interfaced Microfluidic/Electronic Systems for Simultaneous Electrochemical, Colorimetric, and Volumetric Analysis of Sweat. *Sci. Adv.* **2023**, *5*, eaav3294. [[CrossRef](#)] [[PubMed](#)]

258. Li, Y.; Kang, Z.; Kong, L.; Shi, H.; Zhang, Y.; Cui, M.; Yang, D.-P. MXene-Ti₃C₂/CuS Nanocomposites: Enhanced Peroxidase-like Activity and Sensitive Colorimetric Cholesterol Detection. *Mater. Sci. Eng. C* **2019**, *104*, 110000. [[CrossRef](#)]
259. Zeng, Y.; Hu, R.; Wang, L.; Gu, D.; He, J.; Wu, S.-Y.; Ho, H.-P.; Li, X.; Qu, J.; Gao, B.Z.; et al. Recent Advances in Surface Plasmon Resonance Imaging: Detection Speed, Sensitivity, and Portability. *Nanophotonics* **2017**, *6*, 1017–1030. [[CrossRef](#)]
260. Balciunas, D.; Plausinaitis, D.; Ratautaite, V.; Ramanaviciene, A.; Ramanavicius, A. Towards Electrochemical Surface Plasmon Resonance Sensor Based on the Molecularly Imprinted Polypyrrole for Glyphosate Sensing. *Talanta* **2022**, *241*, 123252. [[CrossRef](#)]
261. Kausaite-Minkstimiene, A.; Ramanavicius, A.; Ruksnaite, J.; Ramanaviciene, A. A Surface Plasmon Resonance Immunosensor for Human Growth Hormone Based on Fragmented Antibodies. *Anal. Methods* **2013**, *5*, 4757–4763. [[CrossRef](#)]
262. Zhu, X.; Gao, T. Chapter 10—Spectrometry. In *Nano-Inspired Biosensors for Protein Assay with Clinical Applications*; Li, G., Ed.; Elsevier: Amsterdam, The Netherlands, 2019; pp. 237–264, ISBN 978-0-12-815053-5.
263. Chen, R.; Kan, L.; Duan, F.; He, L.; Wang, M.; Cui, J.; Zhang, Z.; Zhang, Z. Surface Plasmon Resonance Aptasensor Based on Niobium Carbide MXene Quantum Dots for Nucleocapsid of SARS-CoV-2 Detection. *Microchim. Acta* **2021**, *188*, 316. [[CrossRef](#)]
264. Baniukevic, J.; Hakki Boyaci, I.; Goktug Bozkurt, A.; Tamer, U.; Ramanavicius, A.; Ramanaviciene, A. Magnetic Gold Nanoparticles in SERS-Based Sandwich Immunoassay for Antigen Detection by Well Oriented Antibodies. *Biosens. Bioelectron.* **2013**, *43*, 281–288. [[CrossRef](#)]
265. Liu, R.; Jiang, L.; Yu, Z.; Jing, X.; Liang, X.; Wang, D.; Yang, B.; Lu, C.; Zhou, W.; Jin, S. MXene (Ti₃C₂Tx)-Ag Nanocomplex as Efficient and Quantitative SERS Biosensor Platform by in-Situ PDDA Electrostatic Self-Assembly Synthesis Strategy. *Sens. Actuators B Chem.* **2021**, *333*, 129581. [[CrossRef](#)]

Disclaimer/Publisher’s Note: The statements, opinions and data contained in all publications are solely those of the individual author(s) and contributor(s) and not of MDPI and/or the editor(s). MDPI and/or the editor(s) disclaim responsibility for any injury to people or property resulting from any ideas, methods, instructions or products referred to in the content.